

Review of explosive detection methodologies and the emergence of standoff deep UV resonance Raman

Katie L. Gares,[†] Kyle T. Hufziger,[†] Sergei V. Bykov and Sanford A. Asher*

Due to terrorist use of explosive devices, intense interest has been directed towards the development of techniques and instrumentation to detect explosives. A number of analytical techniques are currently under investigation for trace explosive detection. Several methods have been successfully commercialized including colorimetric kits, fluorescence quenching sensors, and ion mobility spectrometers that see widespread field use. A key limitation of all currently utilized field techniques is that they require close proximity or physical interaction with the object being analyzed. The ideal trace explosive detection technique would be able to detect trace amounts of explosives from a distance to ensure personnel safety. Laser-based spectroscopies are the only currently viable techniques that can be utilized to sense trace amounts of explosives at standoff distances. This review compares currently used explosive detection techniques with recently developed standoff methods. We emphasize the development of UV resonance Raman spectroscopy for standoff explosive detection. This work has recently been enabled by advances in laser and spectrometer design. Trace explosive detection has also been advanced by the recently developed understanding of deep UV photochemistry for several explosive molecules. Copyright © 2016 John Wiley & Sons, Ltd.

Keywords: explosive detection; standoff; UV resonance Raman spectroscopy; explosive photochemistry; lasers

Introduction

Interest in explosive detection methodologies has grown in recent years because of the increased use of improvised explosive devices (IEDs).^[1–7] Attacks utilizing explosives are the most common method used in terrorist attacks.^[8] The number of terrorist attacks has increased dramatically from 2004 to 2014, as shown in Fig. 1.^[9]

Figure 1 also shows the large increase in the number of attacks that utilize explosives, bombs, and dynamites.^[9] IEDs and homemade explosives (HMEs) have become the primary threat jeopardizing the safety of civilian and military personnel.^[5,10,11] HMEs are significant threats because the materials used to construct them are easily obtained.

There is a current need to improve security screening methods for explosive detection. For example, in airports, it is important to detect the presence of hidden explosives in luggage, to detect explosive residues on people's hands, and to detect explosives on the aircraft itself.^[7,12] Explosive detection is also needed to monitor vehicle surfaces at security checkpoints, for screening individual people, and for screening mail.^[7,13] These detection methods obviously must sense trace explosive residues that are left by people handling explosives.

There are many different types of explosives that have multiple applications. The most common military explosives are cyclotetramethylenetetranitramine (HMX), pentaerithrityl tetranitrate (PETN), cyclotrimethylenetrinitramine (RDX), and trinitrotoluene (TNT).^[4,13] Military explosive compounds typically contain: O–NO₂ in nitrate esters [PETN, nitroglycerin (NG), ethylene glycol dinitrate (EGDN)], C–NO₂ in nitroaromatics (TNT), and N–NO₂ in nitramines (RDX and HMX).^[13] NG is used in solid rocket propellants.^[4] NG and EGDN are viscous liquid explosives that can be mixed and used in dynamites.^[4,13] Ammonium nitrate (NH₄NO₃), a common fertilizer, is often used in

HMEs.^[4] Solid rocket propellants typically use ammonium perchlorate [NH₄ClO₄ (AP)] as an oxidizer. Plastic explosives include C-4 (composed of RDX and plasticizers) and Semtex-H (composed of RDX and PETN). Plastic explosives have become widely used in terrorist bombings.^[13] Potassium nitrate (KNO₃) and sodium nitrate (NaNO₃) are used in black powder.^[4]

Peroxide-based explosives such as triacetone triperoxide (TATP) and hexamethylene triperoxide diamine (HMTD) have become more popular for terrorists in the recent years because they are easily made from readily available chemicals.^[4,13] These compounds are extremely unstable; the O–O bond rapidly oxidizes making it easy to initiate and explode.^[4,13]

Explosives typically have low vapor pressures (ppb) making them difficult to detect.^[4,6,13–15] Methods for vapor detection need to be able to detect extremely small concentrations and/or sample large volumes.^[4] Furthermore, packaging explosives (i.e. within a plastic bag) will reduce the effective vapor pressure by several orders of magnitude, making detection of explosive vapors much more difficult.^[16]

Non-standoff explosive detection

The 11 September 2001 attack on the USA and the subsequent wars in Afghanistan and Iraq dramatically increased the apparent

* Correspondence to: Sanford A. Asher, Department of Chemistry, University of Pittsburgh, Pittsburgh, PA 15260, USA.
E-mail: asher@pitt.edu

[†] Both authors contributed equally to this work.

Department of Chemistry, University of Pittsburgh, Pittsburgh, PA 15260

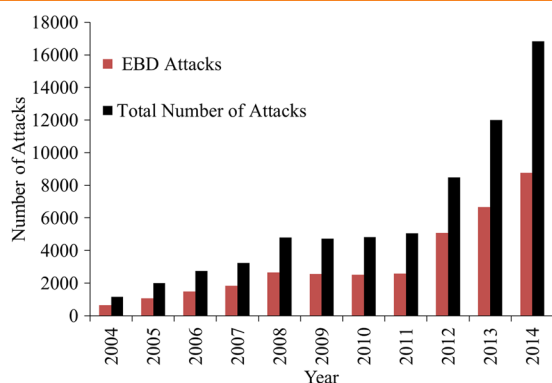


Figure 1. Total number of terrorist attacks worldwide and the number of attacks utilizing explosives, bombs, and dynamites (EBDs) from 2004 to 2014. Figure derives from data in reference.^[9]

need and funding for explosive detection.^[17] The goal of this review is to discuss the leading explosive detection methodologies and to compare them with the emergence of standoff deep UV resonance Raman (UVR) spectroscopy. Several non-standoff methodologies are already widely utilized by law enforcement and military personnel.

Canine olfaction

Canine olfaction is known to be extremely sensitive, and trained dogs have been used for explosive detection since World War II.^[18] Despite the rapid development of explosive detection instrumentation, trained dogs are still one of the most widely employed detection systems because they offer sensitivity, specificity, and directionality, which are found lacking in many portable analytical systems. Limited evidence suggests that canines can sense some analytes at parts per trillion (ppt) levels^[19]; however, there are numerous challenges associated with the use of canine detection. Canine duty time is generally limited to just a few hours a day, and canine sensing effectiveness is a function of training, physical activity, and handler influence.^[20–23] At present, the mechanism of olfaction is not well understood, and it is unclear if trained canines sense the analyte of interest or accompanying impurities present in the explosive material.^[4,24]

Ion mobility spectrometry

Ion mobility spectrometry (IMS) is an analytical technique that sees widespread use in airports worldwide for explosive detection.^[25,26] The technology used in IMS is relatively mature, which facilitates its development for field use.^[27–30] Sample collection typically occurs using surface swabbing. The swab is then rapidly heated to evaporate any adsorbed volatile species. A ‘sniffing’ methodology can also be utilized where air is drawn directly into the IMS spectrometer to be sampled.^[27] Samples introduced into the IMS spectrometer are typically pre-concentrated before being ionized via radioactive ^{63}Ni , electrospray ionization, photo-ionization, or corona discharge, among other approaches.

The ions are then introduced into a drift tube along with a carrier gas, which is typically purified air. An electric field applied across the length of the drift tube propels ions through the field at different characteristic velocities which depend on their mass, charge, and collision cross sections before being detected (Fig. 2). Detection limits for explosive molecules readily reach into the picogram regime.^[1,27] IMS is a widely adopted explosive detection method

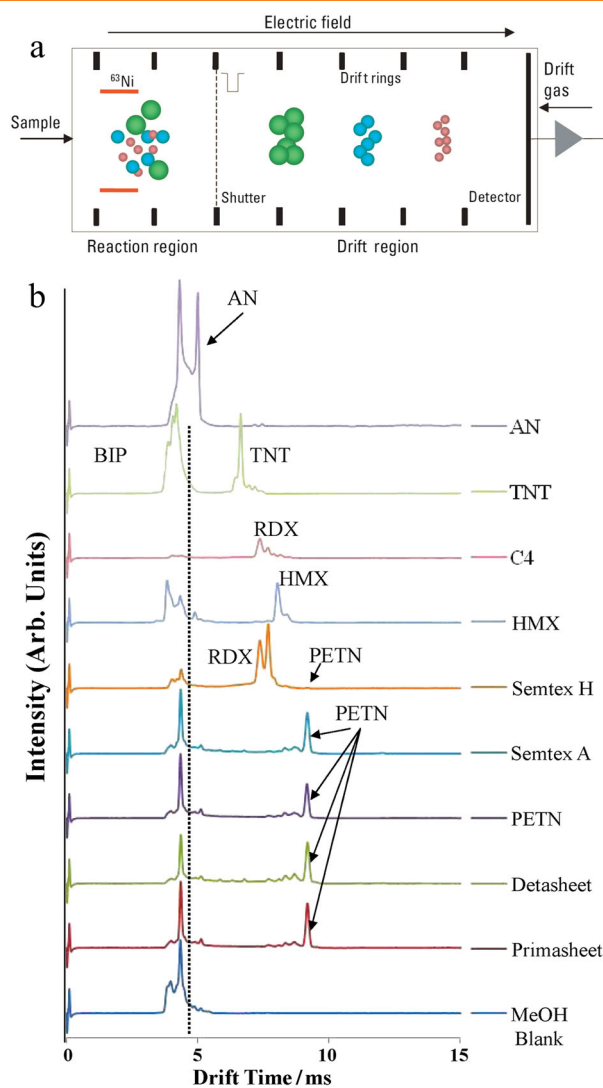


Figure 2. (a) Example of an IMS measurement. First, molecules are introduced into the reaction region to be ionized before being introduced into the drift region to be separated by mass, charge, and collision cross section before being detected. (b) Example spectra of several explosives detected by an ion mobility spectrometer. Figure adapted from references.^[31,32]

because it has been commercialized as small, easy to use instruments that produce results in several seconds.

However, there are several challenges faced by IMS. Because analyte molecules need to be physically drawn into the spectrometer, this precludes the use of IMS for standoff detection. The necessity of physical sample handling also hampers automated screening as well as the screening of large objects. Trace vapor detection is also impeded by the extremely low vapor pressures (ppb) of many explosives.

Colorimetric and fluorimetric

Colorimetric and fluorimetric assays produce spectral changes upon interactions with explosive analytes. Color-based techniques offer low cost, simple to interpret, and instrument-free detection that can be performed by untrained personnel in the field. Three broad categories of color-based detection exist: colorimetric,

fluorescence quenching, and fluorescence activation.^[33,34] Colorimetric-based assays typically function by utilizing Griess and Meisenheimer chemistries to produce brightly colored compounds upon reaction with nitrites (NO_2^-) and nitroaromatics, respectively. In a Griess test, nitrate esters and nitramines are treated with base to release NO_2^- , followed by treatment with sulphanilic acid and an arylamine to produce a bright pink azo dye,^[33] enabling visual detection of RDX, HMX, PETN, NG, and nitrocellulose.^[35]

Alternatively, nitroaromatics such as TNT and dinitrotoluene (DNT) can react with nucleophilic bases to produce brightly colored Meisenheimer complexes with ppm detection limits.^[36] These technologies have been developed as commercially available spray kits for field detection of explosives.^[37] While these tests are rapid, inexpensive, and simple to use, the utilization of colorimetric detection is hampered by its lack of specificity and its moderate sensitivity. The Griess test, for example, can produce false positives if fertilizer, nitrocellulose (commonly found in lacquers), or other sources of NO_2^- have contaminated the interrogated area.

Fluorimetric quenching explosive detection assays typically utilize electron-rich conjugated polymeric substrates, which contain many fluorophores that act as binding sites for explosive molecules.^[33] When the polymer is excited by photon absorption, the excited state involves multiple fluorophores along the polymer chain.^[38,39] If a quenching molecule such as an electron-deficient nitroaromatic is bound to a sampled binding site, the excitation will be quenched. The quenching of multiple fluorophores by a single analyte molecule greatly enhances detection sensitivity.^[40] This has enabled ppb level sensing for TNT, DNT, and dinitrobenzene (DNB).^[41–44] Cumming *et al.* demonstrated a sensor system (Fido) that consists of a chamber containing a fluorescent pentiptycene polymer film, which samples air being drawn through the sensor inlet.^[45] A blue light-emitting diode fluorescence excitation source and a photomultiplier tube (PMT) detect the decrease in fluorescence intensity when explosive analytes bind to the polymer film (Fig. 3). TNT was detected at ppt levels in air as well as in the air surrounding deactivated landmines buried at a DARPA test range. This methodology has been commercialized for handheld explosive detection fluorescence quenching devices for military use.

Fluorescence turn-on methodologies have recently been developed. These sensors function by forming fluorescing species upon reaction with specific explosive molecules. The emission of these fluorophores sensitively reports the presence of explosives. PPM sensitivities for RDX and PETN were reported as well

as ppb sensitivities for TATP and TNT.^[47–49] The broad challenge facing color-based sensors is that each sensor is designed to sense a specific explosive of interest or a single class of explosives. Thus, multiple sensors are required for field detection of explosives. These methodologies are not amenable to standoff detection.

Other methods

In addition to the methods mentioned above, there exist a multitude of other techniques that are currently being investigated for the purpose of explosives detection. These methods include mass spectrometry^[50–52] and neutron techniques^[53] for explosive identification, as well as X-ray and X-ray computed tomography methods for imaging suspected explosive devices in airline luggage.^[54] These analytical methods all have the disadvantage that they need to be placed in direct proximity to the interrogated object in order to analyze its composition.

Standoff explosive detection

Approaching a suspicious object such as a suspected IED is extremely undesirable from a safety standpoint. It is therefore highly desirable to develop standoff methodologies to determine the composition of a sample from a safe distance in order to keep both personnel and instrumentation from harm. Laser-based spectroscopies appear to be the only currently viable standoff detection methods. Standoff spectroscopic measurements have been demonstrated at distances of tens to hundreds of meters.^[55–57] Furthermore, because no physical interaction with the sample is necessary, it is possible to construct instruments that can continually and automatically survey an area (for example, a military checkpoint) and alert an operator if a hazardous analyte is detected. Spectroscopic techniques can be highly selective and can be employed to detect many different analytes of interest. Laser based spectroscopies can also be utilized in chemical imaging methodologies to obtain spatially resolved chemical composition information.^[58–60]

Standoff spectroscopic methods face significant challenges. As the distance from the object being analyzed to the collection optic increases, the amount of light collected will decrease as the inverse square of the distance.^[55] Long-distance measurements typically require the use of large telescopes for light collection, high laser

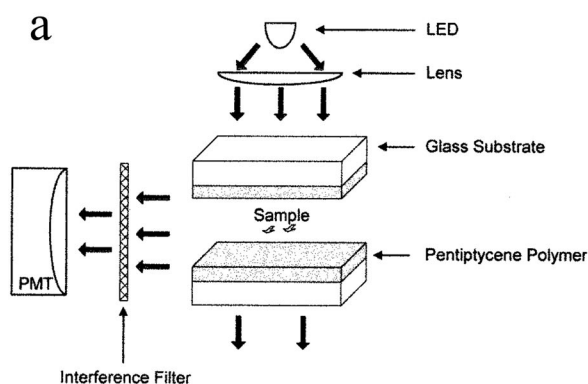


Figure 3. (a) Schematic of the Fido fluorescence quenching explosive sensor originally demonstrated in 2001. (b) Handheld Fido 4A fluorescence quenching instrument. Figure adapted from references.^[45,46]

powers, efficient spectrometers, and long accumulation times. The collected signal intensity increases with excitation power; however, eye and skin-safe field detection requires low laser powers.

LIBS

Laser-induced breakdown spectroscopy (LIBS) has recently been developed as a spectroscopic technique for standoff explosive detection.^[61,62] LIBS utilizes short, high peak power laser pulses to produce dielectric breakdown of the sample surface, resulting in rapid heating and plasma formation.^[63,64] Materials ablated by the plasma spark decompose into multiple smaller molecular, ionic, and atomic species. These species are excited by the plasma and emit photons of characteristic wavelengths. The intensity ratios of the atomic emission lines from C, N, O, and H can be used to infer the original molecular structure stoichiometry by comparing the collected spectra with standard spectra taken of known compounds under similar experimental conditions. LIBS has recently been applied to standoff explosive sensing because it offers the possibility of high signal, long standoff distances, and low spectral accumulation times without the necessity of sample preparation.

Several standoff LIBS instruments for explosive detection have been demonstrated over the past decade. Lopez-Moreno *et al.* demonstrated a portable cart-sized LIBS instrument that detected TNT, RDX, and C-4 deposited on a car door 30 m away (Fig. 4).^[65] A challenge facing field measurements of unknown samples is whether it is possible to identify explosive spectral signatures in the presence of other emitting interferents. The authors developed a spectral analysis method in the form of a flowchart that they used to determine the presence of explosives.

Gottfried *et al.* studied and developed partial least squares and principle component analysis chemometric software to aid in the identification of explosive spectral signatures in the presence of other emitting interferents on different substrate materials.^[66–68] Lucena *et al.* recently constructed an imaging LIBS system that could image fingerprints of explosive molecules at a range of 30 m.^[69] González *et al.* found that they could utilize LIBS to measure TNT and C-4 placed behind transparent sheets of plastic and glass.^[70]

There is interest in combining LIBS and Raman spectroscopy within a single instrument in order to measure both elemental and molecular sample information. Moros *et al.* developed a combined Raman/LIBS instrument that utilized a single 532 nm laser pulse to generate both the LIBS plasma and the Raman scattering, which were collected by a telescope and directed into two separate spectrometers in order to collect both spectra simultaneously.^[71] NH_4NO_3 , RDX, DNT, TNT, PETN, potassium chlorate (KClO_3), and sodium chlorate (NaClO_3) were all measured at a distance of 20 m.

The largest challenge facing the implementation of LIBS as an explosive detection technique for field use is that the LIBS spectra strongly depend upon the detailed experimental conditions. Matrix effects including the emission of molecules on or within the substrate, as well as in the surrounding atmosphere can complicate analyte identification. In addition, organics within the plasma can react to form new species with different spectral emissions. The matrix composition, as well as the incident laser pulse temporal width, energy, and wavelength impact the excited plasma, complicating qualitative and quantitative analyses.^[61] LIBS instruments are also intrinsically eye-unsafe because of their need for high power laser pulses.

Raman

Raman spectroscopy has also been widely utilized for standoff detection. Raman spectra are generated by exciting a sample with a monochromatic light source, normally a laser. Raman spectra detail the intensity of inelastically scattered light as a function of the frequency difference relative to the excitation light.^[72–74] These spectra detail both the structure and environment of the scattering molecule. Thus, Raman spectra serve as sensitive and specific fingerprints that can be used to determine the chemical composition of illuminated samples. Raman spectroscopy can be used as a standoff, highly specific, non-destructive, eye-safe monitor of molecular composition.

In the early 1990s, Angel *et al.* demonstrated a portable visible Raman standoff spectrometer that utilized a visible Ar^+ ion laser to detect several salts including solid state and solution state NaNO_3 at a 17 m distance.^[75] The goal of this study was to develop



Figure 4. Cart mounted standoff LIBS instrument utilized for explosive detection. A Nd:YAG laser produced 350 mJ pulses of 1064 nm light to excite samples including TNT, RDX, and C-4 placed on a car door at 30 m standoff. Figure adapted from Lopez-Moreno *et al.*^[65]

a system capable of measuring contaminants inside of storage tanks at waste disposal sites.

The first demonstrations of standoff Raman for explosive detection were by Carter *et al.* and Sharma *et al.* in the early 2000s.^[55,76] The instrument developed by Carter *et al.* utilized a frequency doubled Nd:YAG laser (532 nm) for excitation and a 20 cm open aperture Cassegrain telescope to collect the scattered light from samples at a 50 m standoff distance. The Raman scattered light from TNT, RDX, PETN, and NH_4NO_3 was collected, dispersed, and detected with a gated, intensified charge-coupled device (ICCD) camera. The authors demonstrated that the use of a short ICCD gate width greatly reduced the background contribution of ambient light and decreased the contribution of sample fluorescence (Fig. 5).

Several Raman standoff studies were performed by the Swedish Defense Research Agency (FOI). Pettersson *et al.* utilized 532 nm excitation coupled with a 15 cm open aperture Cassegrain telescope to collect Raman light from samples such as nitrobenzene (NB), TATP, methyl ethyl ketone peroxide (MEKP), and hexamethylene triperoxide diamine contained within glass containers placed outdoors ~30 m away.^[78] Östmark *et al.* recently demonstrated a standoff visible Raman imaging spectrometer, which utilized 532 nm excitation and a telescope to collect a hyperspectral Raman image of solid chunks of sulfur, DNT, NH_4NO_3 , and TNT placed 10 m away (Fig. 6).^[77] A liquid crystal tunable filter (LCTF) was utilized to transmit only a single narrow wavelength spectral region (~0.25 nm) to be focused onto a CCD camera. The LCTF could be rapidly wavelength tuned to enable efficient hyperspectral image collection. By judiciously selecting and imaging the Raman bands characteristic of each analyte, the different explosives could be easily distinguished in the resulting Raman spectral images.

Collecting Raman spectra of samples within containers can be difficult because the container walls also Raman scatter and interfere with determination of the container contents. Spatially offset

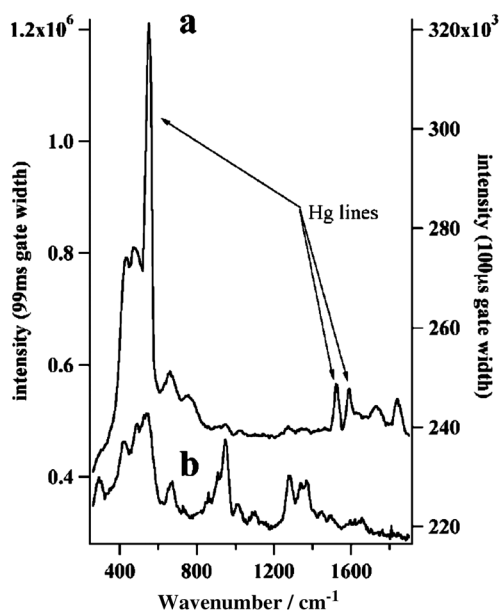


Figure 5. Twenty seven meter standoff Raman spectra of RDX with a (a) 99 ms and (b) 100 μs ICCD gate width. The spectra show strong Hg lines from fluorescent ceiling lamps that appear with longer gate widths. Figure adapted from Carter *et al.*^[55]

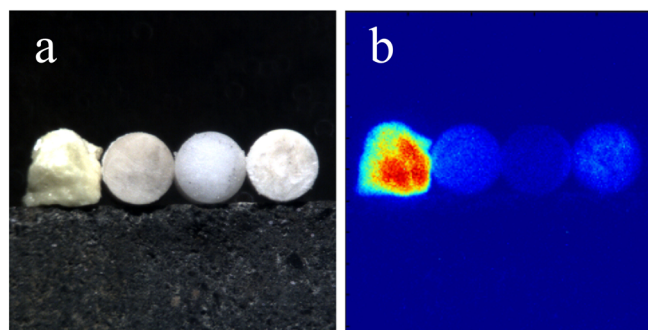


Figure 6. (a) White light image of solid 5 mm diameter sulfur, DNT, NH_4NO_3 , and TNT samples from left to right. (b) Raman spectral image of the samples depicted at left indicating the sum of the measured Raman band intensities. Color indicates relative Raman intensity from low (blue) to high (red). Sulfur Raman scatters much more efficiently than the three other samples, resulting in a bright red feature. Figure adapted from Östmark *et al.*^[77]

Raman spectroscopy (SORS) utilizes a spatial offset between the laser excitation spot and the spot where the collection optic is focused in order to minimize the contribution of Raman bands from the container walls. This increases the relative intensities of the Raman bands of the container's contents.^[80] The principle behind SORS is that Raman scattered light generated by a highly scattering sample powder inside a container is more likely to propagate laterally before it exits the container, compared with Raman light generated by the container wall.^[80] Therefore, as the collection optic is pointed away from the laser excitation, more Raman scattered light from the container contents are observed relative to that from the container wall.

Zachhuber *et al.* recently demonstrated standoff SORS for the analysis of chemicals within containers.^[79,81] A 532 nm laser beam with beam directing optics to produce the spatial offset was utilized to generate Raman scattering in the sample that was then collected by a telescope. Offset Raman spectra were measured of NaClO_3 contained within semi-opaque, high-density polyethylene (HDPE) containers placed 12 m away. At 0 mm offset, the telescope and laser beam are coaxial, and the collected spectra contain Raman bands from both NaClO_3 and HDPE (Fig. 7). However, as the offset between the laser beam and the telescope increases, the HDPE bands diminish in intensity relative to NaClO_3 , and the collected spectra approach that of pure NaClO_3 . The ability to collect Raman spectra through semi-opaque containers can be important for field use in cases where bulk explosive materials are stored within containers.

Misra *et al.* demonstrated that visible Raman spectra can be measured from greater than 100 m standoff distances.^[82] Single 100 mJ pulses of 532 nm light-excited NB, potassium perchlorate, and NH_4NO_3 samples inside sealed glass vials 120 m away (Fig. 8). The Raman scattered light was collected by a 20 cm diameter telescope and focused into a spectrograph. The light was detected by an ICCD camera. Importantly, no cosmic ray removal or baseline correction was necessary before data analysis because of the use of ICCD gating to detect spectra only during the brief time period during the arrival of Raman scattered light in order to minimize spectral interference from ambient light and cosmic rays. High S/N spectra were easily measured with short accumulation times. Collection of high S/N spectra with minimal contributions from spectral interferences is important for field instrumentation in order to enable trace explosives identification.

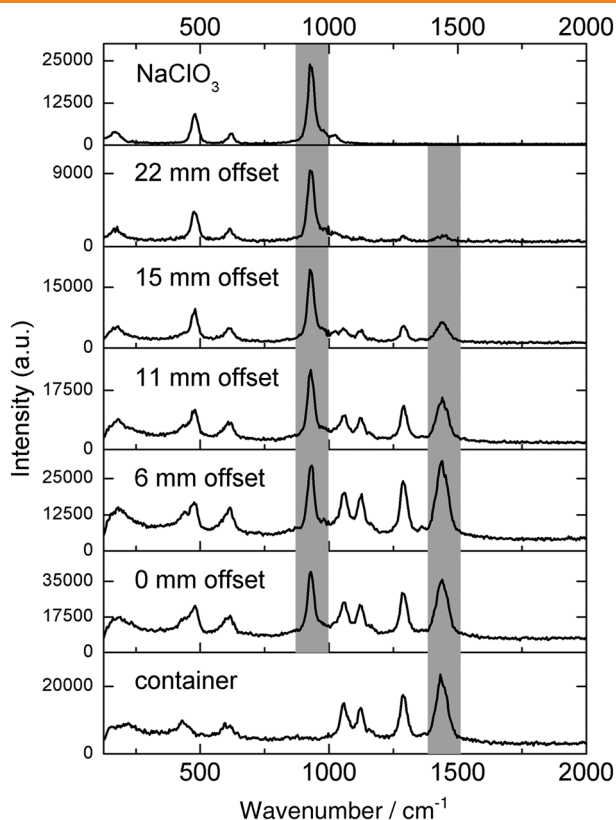


Figure 7. Spatially offset Raman spectra of solid NaClO_3 held within a 1.5-mm-thick high-density polyethylene (HDPE) container at 12 m standoff. Neat NaClO_3 and HDPE are depicted in the top and bottom spectra, respectively. The ratio of NaClO_3 to HDPE Raman bands increase with the spatial offset between the collection optic and the exciting beam. Figure adapted from Zachhuber *et al.*^[79]

Until recently, most standoff excitation studies utilized visible and near-IR wavelength lasers such as Ar and Kr ion lasers, frequency doubled Nd:YAG lasers, and diode lasers because of their widespread availability. In addition, high-quality optics and optical filters, which can be used to reject Rayleigh scattered light, are also easily available for visible and near-IR wavelength excitation. Visibly excited standoff Raman spectroscopy is challenged by sample and impurity fluorescence, which often occurs in the same spectral region as the Raman bands of interest. Intense fluorescence can degrade spectral S/N, which impedes analyte detection. Pulsed laser excitation and gated detection can be utilized to reduce contributions from fluorescence as well as ambient light and cosmic rays. However, the use of pulsed laser excitation significantly increases the eye safety hazards associated with the field standoff measurements.

CARS

Several studies have investigated using nonlinear Raman methods such as coherent anti-Stokes Raman spectroscopy (CARS) for standoff explosives detection.^[83–85] CARS is a nonlinear technique that traditionally utilizes two laser beams to excite a sample. Pump (ω_p) and probe (ω'_p) fields from one beam interact with the Stokes field (ω_s) from a second beam to produce anti-Stokes scattered light (Fig. 9).^[86] The principle advantage of traditional CARS is that a large intensity spatially defined beam of antiStokes Raman scattered light can be generated.^[87] Additionally, because the



Figure 8. Standoff visible Raman spectrometer constructed by Misra *et al.* pointed at samples 120 m away. Figure adapted from Misra *et al.*^[82]

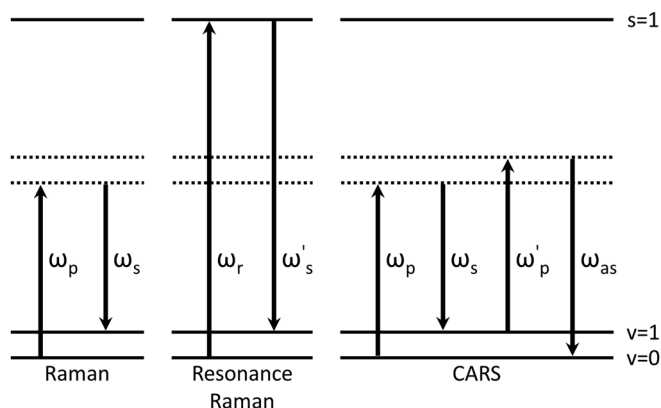


Figure 9. Energy level diagram for Raman, resonance Raman, and CARS.

scattered light occurs at a blue shifted anti-Stokes frequency, there should be little interference from sample fluorescence. However, the precise three field phase matching conditions required makes traditional CARS unsuitable for standoff detection.

Recently, the use of ultrashort femtosecond laser pulses was shown to simplify the phase matching condition of CARS; a single spectrally broad beam can replace the three separate pumps, Stokes, and probe fields.^[88] Bremer *et al.* recently constructed a

single-beam CARS raster-scan imaging spectrometer that was used to measure multispectral images of DNT at $\mu\text{g}/\text{cm}^2$ concentrations at 1 m.^[83] Natan *et al.* developed a single-beam CARS spectrometer that could measure analytes such as nitrate, urea, and RDX from 12 to 50 m away using a 19 cm lens.^[85] The authors demonstrated that RDX could be detected at 24 m with a 3 s accumulation time. Development of standoff CARS instrumentation for field use is impeded due to relatively high laser costs as well as due to eye safety concerns associated with ultrafast laser excitation pulses.

UV Raman spectroscopy of explosives

Advantages of UV excitation

Although visible Raman spectroscopy has been successfully used for standoff detection of bulk amounts of explosives, trace explosives detection will be difficult with visible or near-IR excitation due to the generally small visible or near-IR Raman cross sections that result in low sensitivity. Furthermore, visible and near-IR excitation cannot be used to selectively enhance the resonance Raman spectra of explosives. For visible excitation, Raman bands of explosives have cross sections similar to those of interferents and substrates. This degrades the ability to spectrally differentiate between explosive analytes and interferents.

Excitation in the deep UV ($<260\text{ nm}$) results in an increased selectivity and sensitivity of standoff Raman due to resonance enhancement, the ν^4 dependence of the scattered intensity, and the lack of deep UV interference from fluorescence.^[73,89] Resonance enhancement results in increased Raman intensities from molecules that absorb near or at the excitation wavelength.

Fountain *et al.* and Emmons *et al.* measured the dependence of Raman scattering intensities of NH_4NO_3 and TNT on both the excitation wavelength (from the near IR to the UV) and on the sample thickness.^[2,90] The authors demonstrated that deep UV excitation is advantageous for thin film detection where the increased resonance Raman cross sections increase the observed intensities (Fig. 10). They also showed that the increased Raman intensities associated with resonance enhancement is limited by sample absorption. This absorption limits the penetration depth for the excitation beam.

Visible wavelength excitation results in high Raman intensities for thick explosive samples where there is negligible absorption of the excitation beam. Visible excitation produces Raman scattering from a much greater depth of a thick sample because the laser beam is not strongly attenuated. Visible and near-IR wavelength excitation is advantageous for thick, transparent samples, which are unlikely to be encountered in the field. UV excitation is advantageous for trace explosive detection, which generally involves thin samples.

UV excitation is also beneficial for standoff instrumentation because the higher eye exposure limits for deep UV light allows the use of higher laser powers compared with visible excitation. Carroll *et al.* recently compared the use of 532 and 266 nm excitation for eye-safe standoff detection.^[91] The authors conclude that because the maximum permissible exposure (MPE) set by ANSI is much higher for UV light compared with visible light, higher beam powers can be utilized for UV standoff detection, giving a 130-fold increased detection distance for 266 nm excitation compared with 532 nm. At 266 nm, the photochemical MPE set by ANSI is $3\text{ mJ}/\text{cm}^2$, which allows 1 s of sample illumination with a 10 Hz, 1 mW average power 7 mm diameter beam. The authors calculate that for their instrument, these conditions enable an eye-safe 3 m

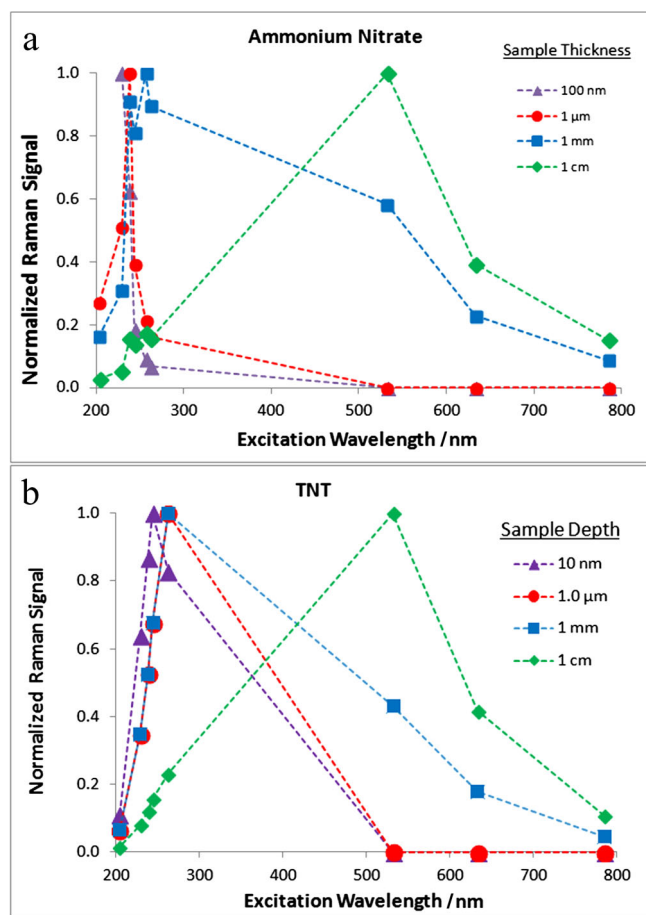


Figure 10. Normalized Raman intensity for the (a) 1044 cm^{-1} band of solid NH_4NO_3 and (b) 1620 cm^{-1} band of solid TNT as a function of sample thickness and excitation wavelength. Figure adapted from Fountain *et al.*^[2]

maximum detection distance for Teflon. It should be noted that protection of personnel against deep UV light is easily accomplished by utilizing glass enclosures and plastic goggles.

UV Raman cross sections

Successful application of standoff UV Raman for trace explosive detection requires development of state-of-the-art UV Raman instrumentation, as well as a deep understanding of UVRR enhancement and the impact of the UV-induced photochemistry of explosive materials on the measured Raman spectra. The spontaneous Raman cross section of a Raman band indicates its efficiency for Raman scattering. This information can be used to calculate the Raman spectral intensities and the spectral detection limits that will be observed for a sample under particular experimental conditions. The Raman cross sections typically increase as excitation occurs within analyte electronic absorption bands. The resonance Raman excitation profile often tracks the square of the absorption band profile,^[92] however, the detailed excitation wavelength dependence can also be very complex.

To optimize standoff Raman measurements of explosives, it is important to understand the dependence of the Raman cross sections on excitation wavelengths for each of the explosive molecules of interest. Generally, excitation at the absorption maxima will yield the highest analyte Raman intensities with the lowest detection limits. Most explosives have their first allowed electronic transitions in

the deep UV below 260 nm.^[92,93] Exciting explosive molecules in the deep UV results in resonance enhancement, which increases the Raman cross sections and the spectral sensitivity.^[2,90,92–96] The UVRR spectra show increased S/N ratios because of these increased Raman cross sections. The increased spectral intensities, however, can be limited by absorption resulting from impurities.^[97] The spectral S/N also increases because of the absence of competing relaxed fluorescence that is present for excitation wavelengths below 260 nm.^[89,92,93] Trace detection of explosives can be optimized by using excitation wavelengths that maximize resonance enhancement.

We determined the optimal trace explosives detection wavelengths from our measurements of the absorption cross sections and Raman cross-section excitation profiles of the explosives NH_4NO_3 , PETN, TNT, HMX, and RDX.^[92–95,98–101] Figure 11 shows the solution absorption spectra of these explosives. All of these explosives absorb at $\lambda < 260$ nm (Fig. 11). PETN and NH_4NO_3 have absorption maxima at ~ 200 nm; deep UV excitation at ~ 200 nm should maximize their resonance enhancement.^[92] For RDX, HMX, and TNT, 229 nm excitation should yield the largest resonance enhancements because of the wavelengths of their absorption maxima. The ~ 200 nm NH_4NO_3 absorption derives from the nitrate (NO_3^-) $\pi-\pi^*$ transition, while the RDX, HMX, and TNT absorptions derive from the $\pi-\pi^*$ transitions of the nitro groups ($-\text{NO}_2$).^[92] The ~ 200 nm PETN absorption derives from the $\pi-\pi^*$ transitions of the O- NO_2 groups.^[92]

We measured the Raman excitation profiles of each of these explosives to determine how the Raman cross section changes with excitation as shown in Figs 12 and 13. Figure 12(a) shows the excitation profile for several NH_4NO_3 Raman bands. The Raman cross sections of the NH_4NO_3 Raman bands increase with excitation frequency and show a maximum at the shortest excitation wavelength of 204 nm.^[93] Figure 12(b) shows the excitation profile for several PETN Raman bands. PETN has an absorption maximum below ~ 200 nm. The excitation profile indicates that the PETN Raman bands show their largest Raman

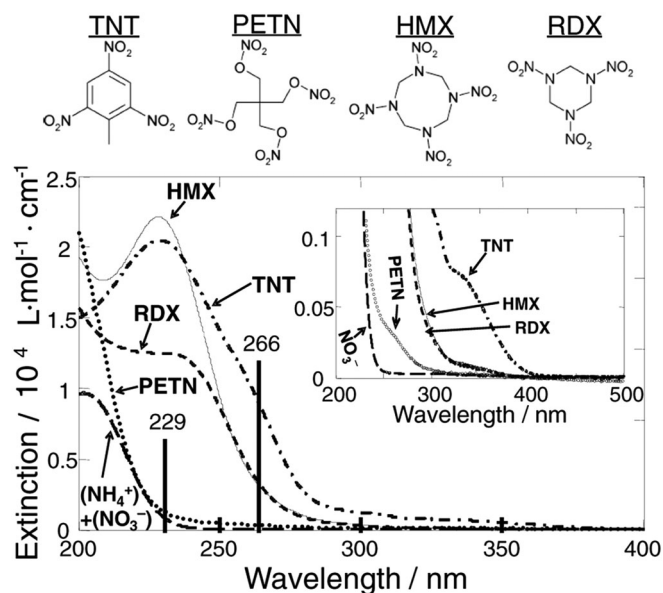


Figure 11. Molar absorptivities of TNT, HMX, RDX, and PETN in acetonitrile (CH_3CN) and aqueous NH_4NO_3 . Sample concentrations were 0.1 mg/mL, and the absorption spectra were measured in 1 mm quartz cuvettes. Chemical structures are also shown. Figure adapted from Tuschel *et al.*^[92]

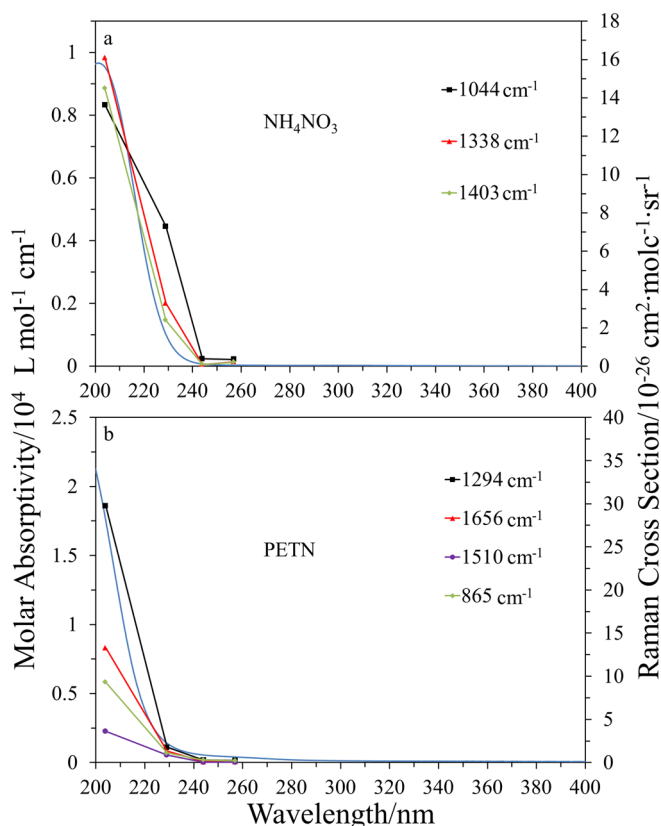


Figure 12. Raman excitation profiles indicate the wavelength dependence of the Raman cross sections: (a) NH_4NO_3 absorption in 77/23% v/v $\text{CH}_3\text{CN}/\text{H}_2\text{O}$ (blue), and the Raman cross sections of the 1044, 1338, 1403 cm^{-1} bands, (b) PETN absorption in CH_3CN (blue), and Raman cross sections for the 1294, 1656, 1510, and 865 cm^{-1} bands. Figure adapted from Ghosh *et al.*^[93]

cross sections with excitation at the shortest wavelength of ~ 204 nm (Fig. 12(b)).^[93]

Figure 13(a) shows the Raman cross-section excitation profiles for several TNT Raman bands. As expected, the Raman cross-section excitation profiles roughly follow the TNT absorption, which shows a maximum at 229 nm and a shoulder at ~ 260 nm (Fig. 13(a)).^[93] A 229 nm excitation gives the greatest resonance enhancement for TNT. The HMX Raman excitation profile is shown in Fig. 13(b). HMX shows an absorption band at ~ 230 nm and another below ~ 200 nm.^[93] The HMX Raman excitation profiles show that the largest Raman cross sections are for excitation within the ~ 230 nm absorption maxima.^[93] Figure 13(c) shows the Raman excitation profile for RDX. RDX shows an absorption band at ~ 230 nm and another below ~ 200 nm.^[93] The Raman excitation profiles show that 204 nm excitation gives the largest Raman cross sections for the RDX 1270 and 1314 cm^{-1} bands.^[93] In contrast, the 1216 and 1586 cm^{-1} RDX bands show Raman cross section maxima at ~ 230 nm.^[93]

Table 1 lists the Raman cross sections of RDX, HMX, TNT, PETN, and NH_4NO_3 in CH_3CN and aqueous solutions for excitation wavelengths between 204 and 257 nm.^[92,93] More detailed tabulations of the Raman cross sections are given elsewhere.^[93] The Raman excitation profiles indicate that TNT and HMX is best excited at ~ 230 nm, while PETN and NH_4NO_3 are best excited at shorter wavelengths at ~ 200 nm. These deep UV Raman cross sections are roughly three orders of magnitude larger than those for visible excitation.^[92]

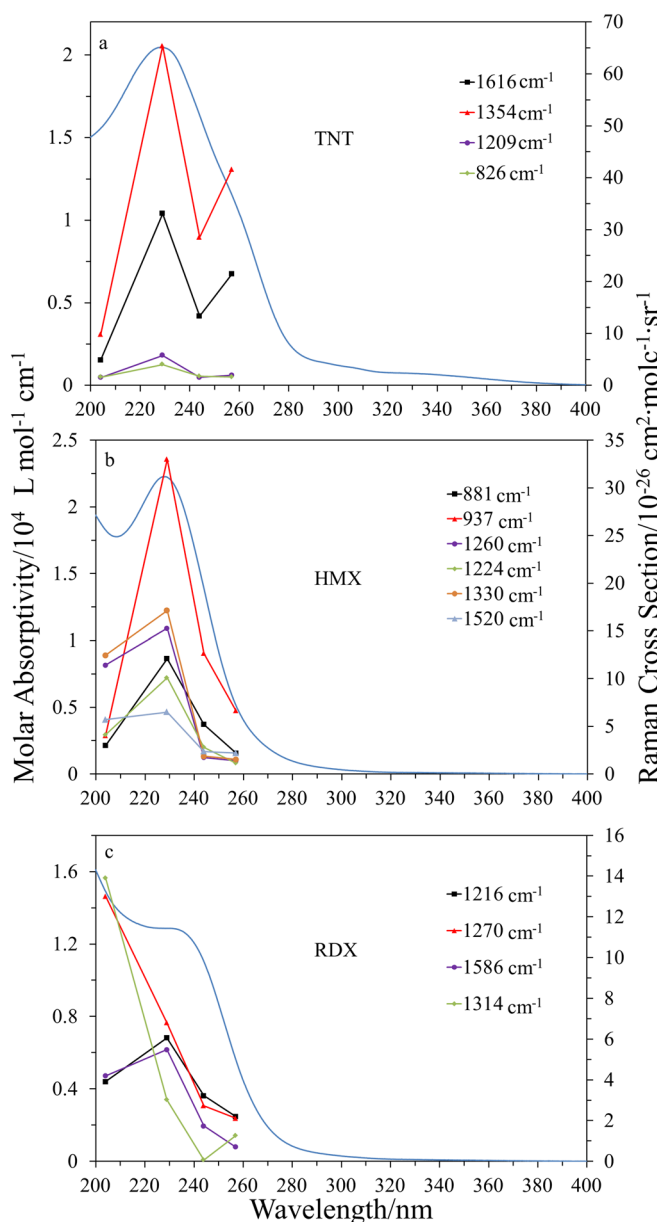


Figure 13. Raman excitation profiles indicate the wavelength dependence of the Raman cross sections: (a) TNT absorption in CH_3CN (blue), and Raman cross sections for the 826, 1209, 1354, and 1616 cm^{-1} bands, (b) HMX absorption in CH_3CN (blue), and Raman cross sections for the 881, 937, 1260, 1224, 1330, and 1520 cm^{-1} bands, (c) RDX absorption in CH_3CN (blue), and Raman cross sections for the 1216, 1270, 1586, and 1314 cm^{-1} bands. Figure adapted from Ghosh *et al.*^[93]

Solution Raman cross sections are relatively easily measured by using an internal standard whose concentration and Raman cross sections are known. In contrast, solid state Raman cross sections are notoriously difficult to measure. We developed a novel method to determine the solid state Raman cross section of NaNO_3 .^[101] We fabricated $\text{NaNO}_3/\text{Na}_2\text{SO}_4$ composite nanoparticles with a defined stoichiometry and utilized the Na_2SO_4 nanoparticles as an internal standard to determine the NaNO_3 Raman cross section.^[101] To create the $\text{NaNO}_3/\text{Na}_2\text{SO}_4$ nanocomposites, we fabricated a close-packed photonic crystal of ~ 80 nm silica nanoparticles. A $\text{NaNO}_3/\text{Na}_2\text{SO}_4$ solution filled the photonic crystal interstices to produce $\text{NaNO}_3/\text{Na}_2\text{SO}_4$ nanoparticles on the silica sphere surfaces.^[101] We measured that the NO_3^- ν_1 symmetric stretching band Raman cross

section for 229 nm excitation is $2.85 \times 10^{-26} \text{ cm}^2 \cdot \text{molecule}^{-1} \cdot \text{sr}^{-1}$, less than half the value of $7.4 \times 10^{-26} \text{ cm}^2 \cdot \text{molecule}^{-1} \cdot \text{sr}^{-1}$ found in our aqueous solution studies.^[101]

Raman cross sections of RDX, HMX, TNT, 2,4-DNT, 2,6-DNT, and NH_4NO_3 were also recently determined by other groups. For example, Emmons *et al.* measured the solution and solid state Raman cross sections of explosives between 532 and 785 nm by using NaNO_3 as an internal standard for solid state measurements, and by using CH_3CN for solution measurements.^[102] Emmons *et al.* also measured UV Raman cross sections of NaNO_3 , PETN, and NH_4NO_3 in solution and in the solid state with excitation between 229 and 262 nm.^[90] They developed a method to study solid state nanoparticle mixtures of explosives where they spray dried a solution containing the explosive analyte and an internal standard onto a heated slide. As the solvent evaporates, crystallized nanoparticles containing the analyte and the internal standard remain.^[90]

They observed significant differences in the Raman cross sections and Raman spectra between solution and solid state samples.^[90] They similarly measured a lower cross section value for solid state NaNO_3 compared with the solution state.^[90] The solid state PETN cross sections increase more than the solution state cross sections as excitation occurs deeper into the UV.^[90]

Photochemistry of explosives

Standoff measurements of explosives will be impacted by the photochemistry that accompanies UV excitation.^[94,95,99,100,103–112]

For example, TNT is well known to photochemically degrade upon exposure to the near UV irradiation from sunlight (< 400 nm).^[103,105,106] This photodegradation results in the formation of multiple photoproducts that result from multiple photolysis pathways. The presence of these photoproducts clearly indicates the previous presence of explosive molecules.

UV excitation within the absorption bands of explosives causes photolysis, which decreases the explosive molecule's concentration such that the analyte Raman spectral band intensities decrease. To quantitate this phenomenon, we have examined the photochemistry of NaNO_3 , TNT, RDX, and NH_4NO_3 ,^[94,95,99,100,112] and are currently studying the photochemistry of PETN.^[113]

Sodium nitrate

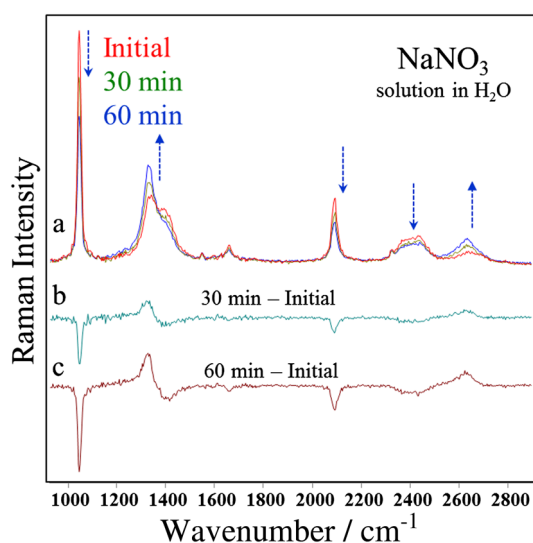
UV excitation into the ~ 200 nm NaNO_3 $\pi \rightarrow \pi^*$ transition causes photolysis of NaNO_3 in both the solid state and in aqueous solution.^[94,112,114–117] Photolysis of NaNO_3 yields nitrite (NO_2^-) and an oxygen radical: $\text{NO}_3^- + h\nu \rightarrow \text{NO}_2^- + \text{O}^\cdot$.^[94,114–117] Similar photochemistry occurs for both 229 and 213 nm excitation within the NO_3^- $\pi \rightarrow \pi^*$ electronic transition.^[94,112]

Figure 14(a) shows the impact of 213 nm photolysis on the UV Raman spectra of an aqueous solution of NaNO_3 . The intensity of the NO_3^- ν_1 symmetric stretching Raman band at 1047 cm^{-1} decreases with increasing irradiation time.^[112] In addition, two new peaks from NO_2^- appear at 1331 and 2654 cm^{-1} (Fig. 14(a)).^[112] Figure 14(b) and (c) shows the difference spectra. Positive features indicate a loss of NO_3^- . The negative features at 1331 and 2654 cm^{-1} indicate formation of NO_2^- .

The photochemistry observed with 213 and 229 nm excitation of solid state NaNO_3 is qualitatively identical to that observed in the solution phase (Fig. 15). NO_3^- is converted into NO_2^- upon excitation with 213 and 229 nm light. Figure 15 shows that as the UV irradiation time of NaNO_3 increases, the ν_1 1068 cm^{-1} NO_3^- Raman band intensity as well as the 2133 cm^{-1} ν_1 overtone intensity

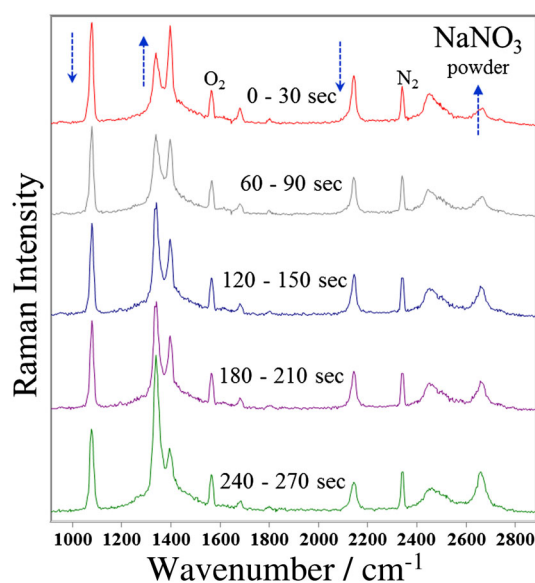
Table 1. Raman cross sections of the explosives NH_4NO_3 , PETN, TNT, HMX, and RDX at different excitation wavelengths

Explosive	Raman bands/ cm^{-1}	204 nm Raman cross sections/ $10^{-26} \text{ cm}^2 \text{ molc}^{-1} \cdot \text{sr}^{-1}$	229 nm Raman cross sections/ $10^{-26} \text{ cm}^2 \text{ molc}^{-1} \cdot \text{sr}^{-1}$	244 nm Raman cross sections/ $10^{-26} \text{ cm}^2 \text{ molc}^{-1} \cdot \text{sr}^{-1}$	257 nm Raman cross sections/ $10^{-26} \text{ cm}^2 \text{ molc}^{-1} \cdot \text{sr}^{-1}$
NH_4NO_3	1044	13.6	7.3	0.40	0.36
	1338	16.1	3.3	0.10	0.23
	1403	14.5	2.4	0.10	0.21
PETN	1294	29.8	1.8	0.30	0.26
	1658	13.3	1.4	0.12	0.12
TNT	1209	1.5	5.8	1.5	1.9
	1354	9.8	65.4	28.5	41.6
	1616	4.9	33.0	13.3	21.4
HMX	937	4.0	33.0	12.7	6.6
	1260	11.4	15.3	1.7	1.4
	1577	6.3	12.6	2.1	0.85
RDX	1270	13.0	6.8	2.7	2.1
	1314	13.9	3.0	0.07	1.3
	1586	4.2	5.5	1.7	0.71

Table adapted from Ghosh *et al.*^[93]**Figure 14.** (a) Time dependent UVRR spectra of an aqueous solution of NaNO_3 irradiated with 213 nm light. (b) Difference spectrum between the irradiated 30 min spectrum and the initial spectrum. (c) Difference spectrum between the irradiated 60 min spectrum and the initial spectrum. Figure adapted from Bykov *et al.*^[112]

decreases.^[112] Formation of the NO_2^- photoproduct is evident from the increasing $\text{NO}_2^- \nu_1$ stretching Raman band at 1331 cm^{-1} and its overtone at 2654 cm^{-1} .^[94,112]

The photolysis of solid state NaNO_3 , which converts NO_3^- to NO_2^- and atomic oxygen, perturbs the lattice causing an upshift in the $\text{NO}_3^- \nu_1$ symmetric stretching band from 1068 to 1078 cm^{-1} (Fig. 16).^[112] As discussed below, the NaNO_3 aqueous solution state quantum yield is measured to be $\phi \sim 0.04$, while the constrained solid state quantum yield is much smaller, $\phi \sim 10^{-8}$. NaNO_3 photolysis yields the resonance enhanced strong Raman bands of NO_2^- photoproduct. Detection of NO_2^- bands may indicate previous presence of NO_3^- derivatives (see below).

**Figure 15.** Time-dependent 213 nm UVRR spectra of solid state NaNO_3 . Incident irradiance on the rotating solid state NaNO_3 sample is $\sim 130 \text{ mW/cm}^2$. The spectra were measured by using 30 s accumulation times. Spectra are scaled to the stretching band of molecular N_2 from air. Figure adapted from Bykov *et al.*^[112]

TNT

TNT photodegrades upon exposure to near-UV ($< 400 \text{ nm}$) irradiation from sunlight through multiple pathways as shown by Clark *et al.* and Kunz *et al.*^[105,106] TNT shows weak UV absorption in the near UV.^[95] TNT excited deeper into the UV, for example, at 229 nm forms similar photoproducts as seen in sunlight illumination studies.^[95] This photolysis leads to photoproducts consisting of an aromatic ring with amine, hydroxyl, and carboxylic acid substituents.^[106] Some of the initial sunlight photolysis photoproducts include 4-amino-2,6-dinitrotoluene, 2-amino-4,6-dinitrotoluene, and 3,5-dinitroaniline (3,5-DNA).^[105]

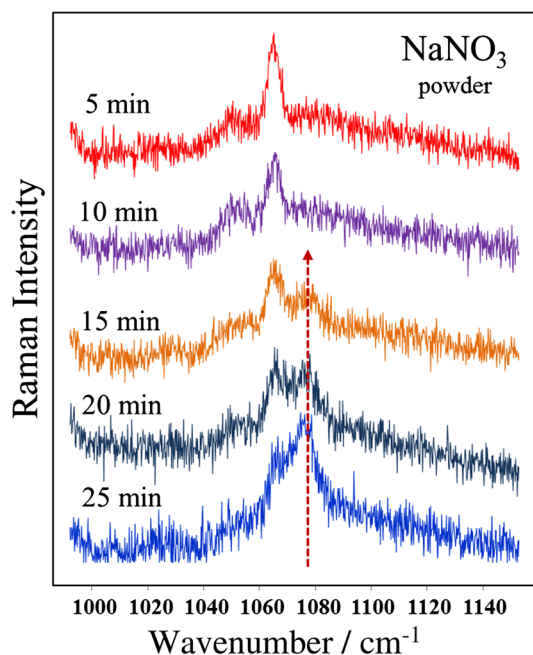


Figure 16. A 2.2 m standoff 213 nm UVRR spectra of solid state NaNO_3 ($\sim 100 \text{ mg/cm}^2$). The spectral accumulation time was 5 min. Figure adapted from Bykov *et al.*^[112]

We studied the 229 nm photochemistry of TNT in both the solution and solid states (Fig. 17). All of the original TNT UVRR bands decrease as the irradiation time increases (Fig. 17(a)). The Raman band at 1210 cm^{-1} selectively decreases and disappears over time, indicating the complete photolysis of TNT. The 1210 cm^{-1} Raman band, which is a TNT marker band, derives from a symmetric aromatic ring breathing mode whose origin requires the symmetry of the TNT aromatic ring.^[92,95,118,119] This band intensity is directly proportional to the TNT concentration in the illuminated sample.

Figure 17 shows that even after the total disappearance of this TNT marker band, the other strong Raman bands appear to remain. These include the 1357 cm^{-1} $-\text{NO}_2$ symmetric stretching band and the 1549 cm^{-1} and the 1622 cm^{-1} $-\text{NO}_2$ asymmetric stretching coupled with aromatic ring stretching bands.^[92,95] These Raman bands derive from photoproducts with similar resonance enhanced bands that closely overlap the original TNT bands. Thus, a TNT-like UVRR spectrum appears to persist even after the true TNT is completely photolyzed.^[95] The persistence of these bands enables us to detect the TNT original analyte even after it is completely photolyzed.^[95] We see very similar photochemistry during the solid state photolysis of TNT (Fig. 17(b)). As discussed below, TNT photodegrades with a solution state quantum yield of $\phi \sim 0.15$.^[95]

RDX

RDX in the condensed and gas phases is known to photodegrade when exposed to UV light.^[99,103,108–111,120–122] The initial stages of RDX photolysis in both the condensed and gas phases involve an N–N bond scission that generates neutral NO_2 .^[103,108–111,121,122] The condensed phase photolysis also generates the mono-, di-, and tri-nitroso derivatives of RDX.^[110] Bernstein *et al.* studied UV RDX photolysis in the gas phase and showed formation of gaseous photoproducts such as nitrogen oxide (NO).^[108,109,121] Bernstein *et al.* utilized femtosecond laser pump-probe techniques and matrix-assisted laser desorption to study the photolysis mechanism of RDX.^[108,109,121]

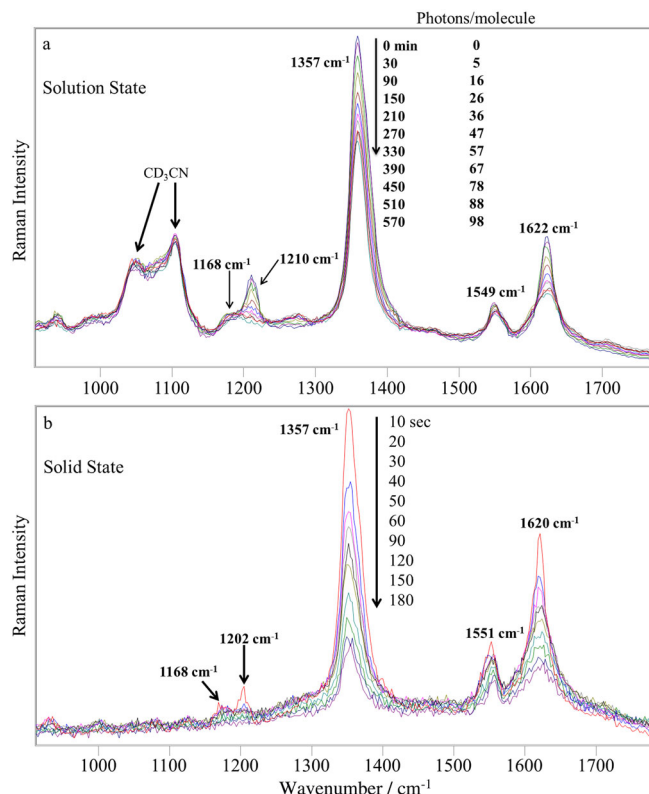


Figure 17. (a) Time-dependent UVRR spectra of 1 mg/mL TNT in CD_3CN irradiated with 10 mW 229 nm light as a function of the number of absorbed photons/molecule. The CD_3CN Raman bands were not subtracted. (b) Time-dependent UVRR spectra of solid state TNT on MgF_2 powder (0.06% w/w TNT) irradiated with 10 mW of 229 nm light. Figure adapted from Gares *et al.*^[95]

We recently studied the UVRR 229 nm photochemistry of RDX in both the solution and solid states (Figs 18 and 19).^[99] We find that RDX has a $\sim 35\%$ photodegradation quantum yield upon exposure

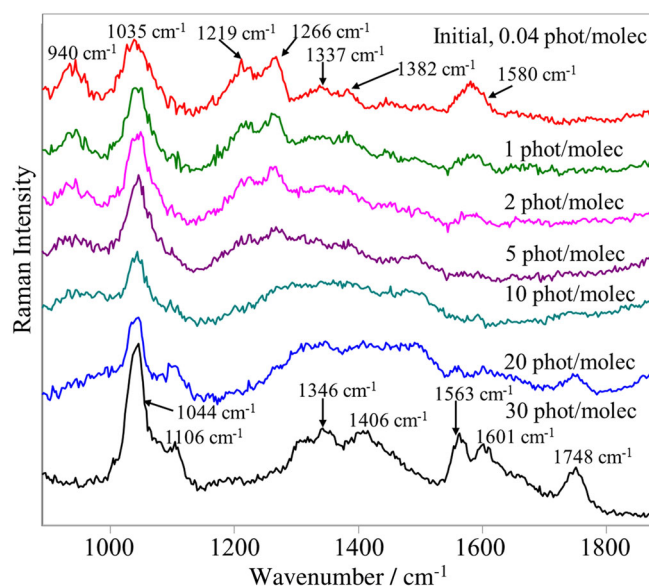


Figure 18. Time dependence of UVRR spectra of 3 mg/mL RDX in CD_3CN solution irradiated with 17 mW of 229 nm light. The CD_3CN and quartz Raman bands were subtracted. Figure adapted from Gares *et al.*^[99]

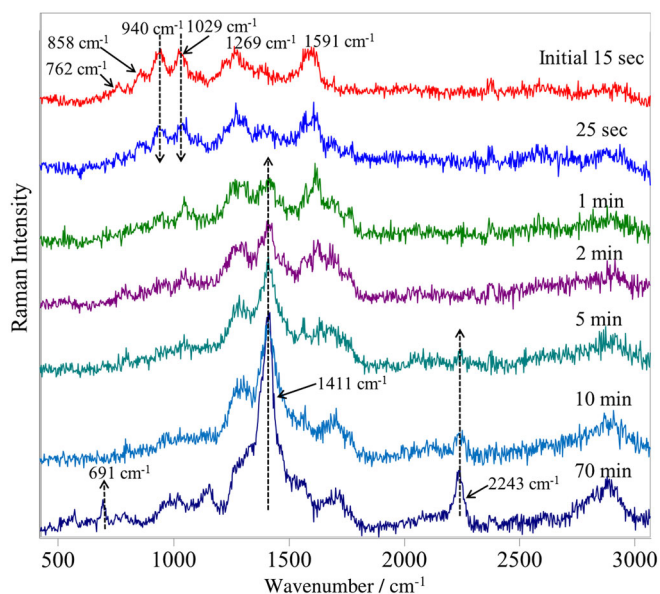


Figure 19. Time dependence of UVRR spectra of solid state RDX on MgF_2 powder (<1% w/w RDX) irradiated with 4.2 mW of 229 nm light. The sample was spinning during excitation. Figure adapted from Gares *et al.*^[99]

to 229 nm light.^[99] Figure 18 shows UVRR spectra that indicate that photodegradation of RDX in CD_3CN solution increases with the number of photons absorbed. The 940 cm^{-1} Raman band, which derives from a vibration containing N–N stretching,^[92,93,99,123] significantly decreases after absorption of ~5 photons per molecule. This indicates photochemical N– NO_2 bond cleavage and a loss of the $-\text{NO}_2$ group. The 1580 cm^{-1} band, which derives from O–N–O stretching,^[92,93,99,123] similarly disappears, further indicating loss of the $-\text{NO}_2$ groups. New photoproduct bands appear as additional photons are absorbed. The dominating photoproduct band at 1044 cm^{-1} in the 30 photon per molecule spectrum likely results from the ν_1 symmetric stretching vibration of a NO_3^- photoproduct,^[94,99] because NO_3^- is a known RDX photolysis photoproduct of the solution state.^[110,124] As discussed below, the RDX solution state quantum yield is high at $\phi \sim 0.35$.

Figure 19 shows the time dependence of the UVRR of solid state RDX. As in the solution state, the 940 cm^{-1} N–N stretching band decreases and disappears during the initial excitation, again indicating cleavage of the N– NO_2 bond and loss of the NO_2 .^[99] The 5 min spectrum shows a photoproduct Raman band at 2243 cm^{-1} that we assign to a $\text{C}\equiv\text{N}$ stretching vibration.^[99] At longer irradiation times, photoproduct Raman bands appear at 691 and 1411 cm^{-1} .

We studied the later stages of RDX photolysis by irradiating ~1 mg of RDX deposited on a stationary quartz slide.^[99] We observe UVRR bands at 1374 and 1654 cm^{-1} that resemble the 'D' and 'G' bands of graphitic/amorphous carbon nitride-like species.^[100,125–128] We also observed a 2243 cm^{-1} $\text{C}\equiv\text{N}$ stretching vibration, which is commonly seen in graphitic/amorphous carbon nitride-like species.^[125,127,129] Extensively photolyzed samples of RDX also show a 691 cm^{-1} Raman band that we assign to the CNC in plane bending vibration also seen in carbon nitride-like species.^[126] The 1411 cm^{-1} band was assigned to breathing modes of sp^2 atoms in ring structures.^[125,127] Extensive photolysis of RDX appears to give rise to graphitic/amorphous carbon nitride species.^[99]

Ammonium nitrate

The photochemistry of solid state NH_4NO_3 dramatically differs from that of NaNO_3 , which, as shown previously, simply forms NO_2^- and atomic oxygen. We are presently attempting to understand the solid state NH_4NO_3 photochemical mechanisms and its reaction products. We are attempting to clearly differentiate between the UV photochemistry and the thermal decomposition reactions of NH_4NO_3 . It should be noted that thermal decomposition can be directly induced by laser irradiation of absorbing samples without requiring any intermediate photochemical processes.

The thermal decomposition of NH_4NO_3 was previously studied.^[130–134] An initial decomposition step involves an endothermic reaction where NH_4NO_3 dissociates to nitric acid and ammonia.^[130–132,134] An exothermic reaction can decompose NH_4NO_3 into nitrous oxide and H_2O .^[130–132,134] Multiple thermal decomposition pathways can give rise to gaseous ammonia (NH_3), nitrous oxide (N_2O), nitrogen dioxide (NO_2), nitric oxide (NO), nitrogen (N_2), oxygen (O_2), and H_2O .^[130,132]

UV photolysis of aqueous solution state NH_4NO_3 is rather simple (Fig. 20).^[115,135] As discussed previously, NO_3^- in aqueous solution is photolyzed into NO_2^- and an oxygen atom: $\text{NO}_3^- + h\nu \rightarrow \text{NO}_2^- + \text{O}$.^[89,114–117,135] Figure 20 shows the UVRR photodegradation spectra of an aqueous NH_4NO_3 solution irradiated for 30 and 60 min with 213 nm light. The spectral changes are essentially identical as for the photodegradation of NaNO_3 (Fig. 14).^[112] The intensity of the $\text{NO}_3^- \nu_1$ vibration at 1047 cm^{-1} and its overtone at 2096 cm^{-1} decreases as the irradiation time increases.^[112] Two new photoproduct bands appear at 1331 and 2654 cm^{-1} , which result from NO_2^- formation.^[112] The solution state photochemistry of NaNO_3 and NH_4NO_3 are identical, forming NO_2^- as the photoproduct.

The UV-induced decomposition of solid state NH_4NO_3 (Fig. 21) differs dramatically from that of NaNO_3 (Fig. 15). Figure 21 shows the UVRR spectra of solid state NH_4NO_3 irradiated with 213 nm light. We observe no change in the NH_4NO_3 UVRR spectrum upon irradiation.^[112] We see no evidence for formation of NO_2^- . However,

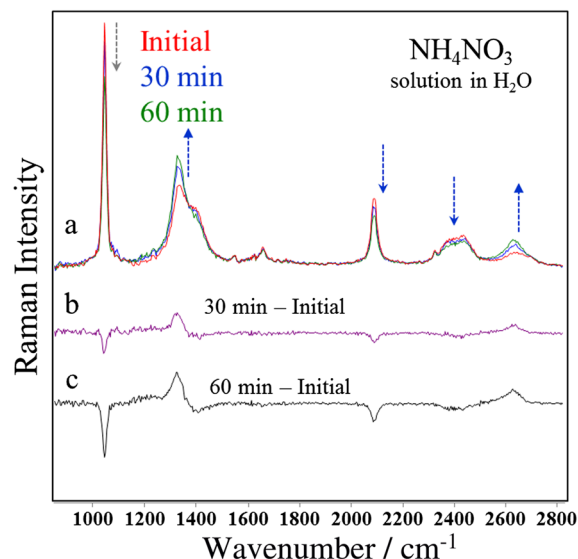


Figure 20. (a) Time-dependent UVRR spectra of an aqueous solution of NH_4NO_3 irradiated with 213 nm light. (b) Difference spectrum of the irradiated 30 min spectrum and the initial spectrum. (c) Difference spectrum of the irradiated 60 min spectrum and the initial spectrum. Figure adapted from Bykov *et al.*^[112]

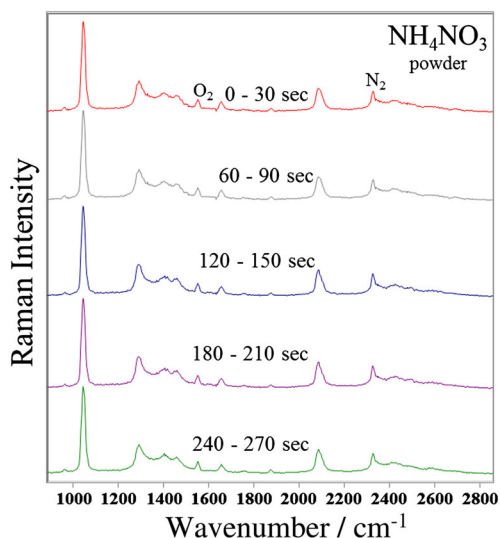


Figure 21. Time-dependent 213 nm UVRR spectra of solid state NH_4NO_3 . Incident irradiance on the rotating sample is $\sim 130 \text{ mW/cm}^2$. UVRR was measured with a 30 s accumulation time. Spectra are scaled to the stretching band of molecular N_2 of air. Figure adapted from Bykov *et al.*^[112]

the weight of our solid NH_4NO_3 samples decrease linearly with illumination time.^[112] We see that the laser beam forms holes in the NH_4NO_3 sample. We presume that the UV-induced decomposition of NH_4NO_3 leads to gaseous products.^[112] We calculate an effective quantum yield for solid state NH_4NO_3 of $\phi \sim 0.20 \pm 0.02$, far greater than for solid state NaNO_3 .^[112] We see that the initial gaseous products formed condense on adjacent container walls into crystals of NH_4NO_3 .

PETN

Thermal decomposition of PETN has been well studied.^[136–139] The initial decomposition step of PETN in the solid state is cleavage of the O– NO_2 bond forming an alkoxide and a nitronium ion.^[136–139] Thermal decomposition can also yield gaseous products such as NO , NO_2 , N_2O , CO , and so on.^[138] PETN decomposition by UV excitation has a similar initial photolysis step as the thermal decomposition at elevated temperatures. The initial step in photochemical decomposition by UV light involves scission of the O– NO_2 bond yielding the alkoxide and nitronium ion.^[103,104] We are currently studying the 229 nm photochemistry of PETN. We measure a solution state quantum yield for PETN of $\phi \sim 0.08$.^[113]

Determination of photoproducts and quantum yield

High-performance liquid chromatography–high-resolution mass spectrometry (HPLC–HRMS) was used to separate and determine the photoproducts of TNT and RDX (Table 2). Table 2 shows the photoproducts along with the measured quantum yields of the explosives studied. For TNT, the initial photoproducts formed in solution are 2-amino-4,6-dinitrotolulene, 3,5-DNA, and 2,5-DNP (Table 2).^[95] 2-amino-4,6-dinitrotoluene and 3,5-DNA, are also observed in near-UV excitation sunlight studies.^[105,106] Similar initial photoproducts are observed in the photolysis of solid state TNT.^[95]

The major initial photoproducts formed during solution RDX photolysis are its nitroso derivatives hexahydro-1-nitroso-3,5-dinitro-1,3,5-triazine (MNX), hexahydro-1,3-dinitroso-5-nitro-1,3,5-triazine (DNX), and hexahydro-1,3,5-trinitroso-1,3,5-triazine (TNX).^[99] NO_3^- is a dominant photoproduct observed with HPLC–HRMS.^[99]

Gas chromatography mass spectrometry (GCMS) shows that formamide is another dominant photoproduct.^[99]

As discussed previously, UVRR studies of NaNO_3 showed that NO_2^- was the dominant photoproduct from NO_3^- in aqueous solutions and from solid state NaNO_3 .^[94] Table 2 shows the photolysis quantum yield values determined for NaNO_3 , TNT, RDX, NH_4NO_3 , and PETN. The NaNO_3 aqueous solution state 229 nm quantum yield was determined to be $\phi \sim 0.04$, while the solid state quantum yield was calculated to be $\phi \sim 10^{-8}$.^[94] The solid state quantum yield of NaNO_3 is dramatically decreased compared with that in the solution state due to constraints by the lattice.^[94] The solid state quantum yield for NH_4NO_3 was calculated to be $\phi \sim 0.20 \pm 0.02$.^[112] The solution state quantum yield for TNT was calculated to be 0.15.^[95] RDX has a much higher photolysis quantum yield of 0.35.^[99] We calculated a solution state quantum yield for PETN of $\phi \sim 0.08$.^[140]

An understanding of the explosive analyte UVRR photochemical spectral changes enables improved determination of trace analytes. Determination of the time dependence of the UVRR increases the information content of the spectra. Detection of characteristic photochemical products can be used to identify precursor analytes.

UV Raman standoff detection

Several groups have begun exploring the feasibility of standoff UV Raman for explosive detection.^[141–146] Hug *et al.* (Photon Systems Inc.) and Bhartia *et al.* (Jet Propulsion Laboratory/Caltech) have developed portable UV Raman instrumentation utilizing small transverse excited hollow cathode 248 nm NeCu lasers.^[141–143] Waterbury *et al.* (Alakai Defense Systems) have recently constructed a truck mounted UV Raman system for standoff detection.^[144]

The Swedish Defense Research Agency has developed deep UV Raman instruments for standoff detection. Ehlerding *et al.* constructed instruments that utilized deep UV excitation generated by an optical parametric oscillator pumped by the third harmonic of a Nd:YAG laser.^[145] Scattered light was collected by a 13 cm telescope at a 1.6 m standoff distance. The Raman light was dispersed by a single spectrograph and detected by an ICCD. Vapor phase TNT and DNT were detected with 100 s accumulation times. Nitromethane (NM) was also measured outdoors at a 13 m standoff distance.

Reichardt *et al.* constructed an instrument that used 244 nm excitation for the detection of TNT that employed a conventional Czerny–Turner spectrograph with an ICCD detector.^[146] The authors utilized their measured spectral S/N ratios for standoff measurements to estimate the accumulation times necessary to detect TNT. They concluded that detection of $>6 \mu\text{g/cm}^2$ amounts of TNT at $\sim 100 \text{ m}$ standoff distances would require $>10 \text{ s}$ accumulation times.

Advances in UV Raman instrumentation are aiding the development of standoff UV Raman methods for trace explosive detection. While visible and near-IR Rayleigh rejection optical filter technology is mature and relatively inexpensive, commercialized deep Rayleigh rejection filters have much poorer performance with low out-of-band transmission, as well as insufficient cutoff band edge steepness. This has previously necessitated the use of multistage spectrometers with low light throughput.

We recently developed a novel high throughput, high dispersion deep UV Raman spectrometer. This spectrometer consists of a high efficiency filter stage monochromator and a high dispersion

Table 2. Photochemistry of TNT, NaNO₃, RDX, PETN, and NH₄NO₃ along with the measured quantum yields

Explosive molecule	TNT	NaNO ₃	RDX	NH ₄ NO ₃	PETN
Proposed solution state photoproducts	2-amino-4,6-dinitrotoluene 3,5-dinitroaniline (3,5-DNA) 2,5-dinitrophenol (2,5-DNP) 	Nitrite (NO ₂ ⁻)	MNX DNX TNX NO ₃	Nitrite (NO ₂ ⁻)	Not yet determined
Solution state quantum yield (ϕ)	0.015	0.04	0.35	0.04 [†]	0.08
Solid state quantum yield	Not yet determined	10 ⁻⁸	Not yet determined	0.20	Not yet determined

Figure adapted from references.^[94,95,99,112,113]
[†] Estimated value. We expect a similar quantum yield for all solution state nitrates.

Echelle spectrograph (0.04 nm/mm dispersion at 229 nm). This high dispersion allowed us to open the entrance slit to 1 mm, while maintaining a spectral resolution of $\sim 10 \text{ cm}^{-1}$ full width half max. The use of a 1 mm wide entrance slit results in a ~ 35 -fold throughput increase compared with previously UV-optimized Raman spectrographs.^[147] We utilize this spectrograph in a prototype standoff deep UV Raman spectrometer we are developing.^[112] We also developed novel deep UV Rayleigh rejection filters and Raman imaging optics as discussed in detail below.

The development of standoff deep UV Raman instruments has also been slowed by the lack of suitable deep UV laser sources. Current UV Raman measurements mainly utilize Nd:YAG 3rd (355 nm), 4th (266 nm) and 5th (213 nm) harmonics, the second harmonics of visible Ar⁺ ion laser lines at 257, 248, 244 and 229 nm, and UV-tunable (193–240 nm) harmonics of Ti:Sapphire tunable lasers.^[148] For wavelengths below 244 nm, these lasers produce < 20 mW

output power. These lasers are large, heavy, require water cooling, and are relatively inefficient. High-power low-duty cycle excimer lasers, like ArF at 193 nm and KrF at 248 nm, require use of highly poisonous and reactive halogens. High average power, portable, and easy to operate UV lasers are required for standoff Raman instruments.

In collaboration with UVISIR Inc., we recently developed a novel, compact, acousto-optically Q-switched diode-pumped solid state intracavity-frequency tripled Neodymium-doped Yttrium Vanadate (Nd:YVO₄) laser capable of producing up to 100 mW of quasi-CW 213 nm light (Fig. 22). The light is generated as 15 ns pulses at a 30 kHz repetition rate.^[112] We utilized this new laser in a prototype standoff deep UV Raman instrument. We monitored the UVRR spectra of solid and solution nitrate species utilizing our lab-built Echelle deep UV Raman spectrometer.^[112] The laser beam size was ~ 2 mm in diameter at the sample ($\sim 30 \text{ mW/cm}^2$), and Raman scattered

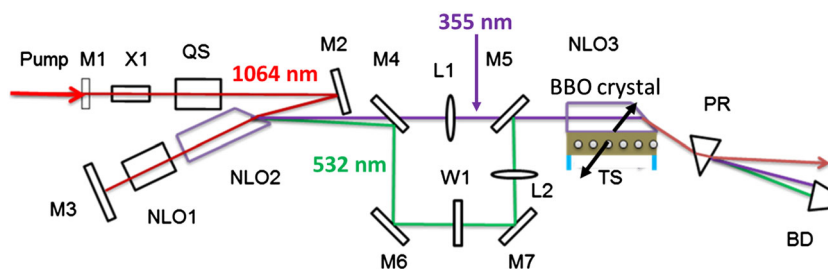


Figure 22. Optical diagram of the compact 213 nm diode-pumped solid state laser. M1–M3 – mirrors, X1 – NdYVO₄ laser crystal, QS – Q-switch, NLO1 – second harmonic crystal, NLO2 – third harmonic crystal, NLO3 – fifth harmonic crystal, M4–M7 – 532/355 separator, L1 – focal lens for 355 nm laser, L2 – focal lens for 532 nm laser, PR – prism, BD – beam dump, W1 – half-wave plate for 532 nm light, TS – translation stage. The BBO crystal is constantly moving at 50 $\mu\text{m/s}$. Figure adapted from Bykov *et al.*^[112]

light was collected by a 5 cm plano-convex lens. At a ~ 2.2 m stand-off distance, we were able to easily monitor the NO₃⁻ symmetric stretching band of 1 mg/cm² NaNO₃ powder spread on a metal surface (Fig. 23) and of 20 μM aqueous solutions of NaNO₃ (Fig. 24).

We monitored the 1065 cm⁻¹ ν_1 NO₃⁻ symmetric stretching band of solid NaNO₃ for different amounts of solid NaNO₃ per cm² (Fig. 23).^[112] We are able to clearly detect the 1065 cm⁻¹ Raman band of solid NaNO₃ at ~ 1 mg/cm² with a 60 s accumulation time. We estimate a ~ 100 $\mu\text{g/cm}^2$ detection limit for 1 min accumulation times for the ν_1 symmetric stretching vibration of solid NO₃⁻.^[112]

We also monitored the 213 nm excited ν_1 symmetric stretching vibration of NO₃⁻ at ~ 1044 cm⁻¹ for solution state NH₄NO₃ at different concentrations (Fig. 24). The 1044 cm⁻¹ band is detectable for 20 μM solutions with 10 s accumulation times.^[112] For the most concentrated 2 M NH₄NO₃ sample, the excitation beam is completely absorbed by a thin surface layer of solution. As the NH₄NO₃ concentration decreases, the beam penetration depth into the sample increases, yielding a larger sampled volume. The number of irradiated molecules therefore remains constant even as the concentration decreases by 4 orders of magnitude, resulting

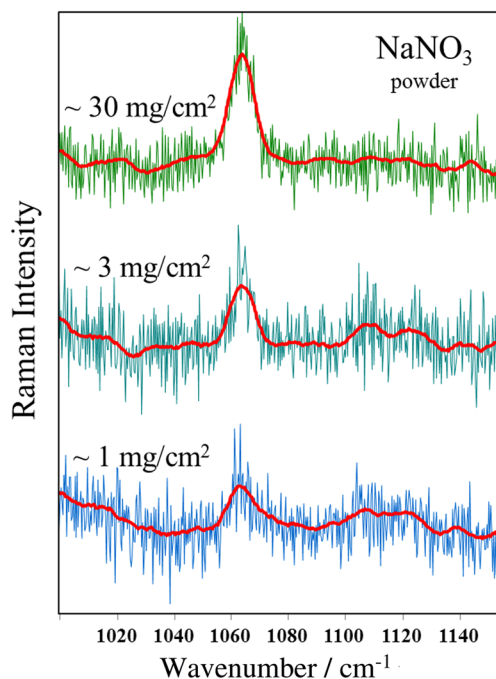


Figure 23. A 2.2 m standoff 213 nm UVRR spectra of different amounts of solid NaNO₃ powder. Spectra were accumulated for 60 s, and the irradiance is ~ 30 mW/cm². The smoothed (Savitzky–Golay) and raw spectra are overlaid. Figure adapted from Bykov *et al.*^[112]

in very similar 1044 cm⁻¹ band measured Raman intensities over a large concentration range.

We are developing a standoff UV Raman wide-field imaging instrument for trace explosive detection. Spectral imaging techniques are powerful because they can be used to determine the location of an analyte of interest on the surface of an object.^[58] Spectral images are traditionally measured by using a raster scanning method where a focused laser illuminates an array of small spatial regions across the surface of the sample. Raman spectra are measured at each spatial region, and a hyperspectral image is calculated from the set of individual raster-scanned spectra. The major disadvantage of raster scanning is that large numbers of individual spectra must be measured. The number of spectra required depends on the size of the surface and the desired spatial resolution.

Alternatively, wide-field imaging instruments can be fabricated to simultaneously collect spectral information from the entire sample surface. Instead of utilizing a focused laser beam, an expanded beam illuminates the entire sample surface. The intensity of a single Raman spectral region is then measured at each point on the surface simultaneously. One benefit of wide-field imaging techniques is that they can be more time efficient and improve hyperspectral image S/N under conditions where the excitation power is not limiting.^[149]

Wide-field imaging instruments typically utilize a wavelength selective optical device that selects a narrow spectral region to be

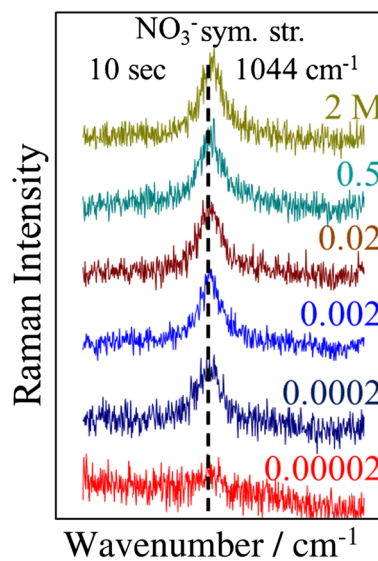


Figure 24. A 2.2 m standoff 213 nm UVRR spectra of aqueous NH₄NO₃ solutions at different concentrations in a 1 cm path length cuvette. Spectra were accumulated for 10 s. Figure adapted from Bykov *et al.*^[112]

detected by a CCD camera. Fiber optic arrays can also be coupled to traditional dispersive spectrometers and used for imaging.^[58,150] LCTFs, acousto-optic devices, and thin film filters are traditionally used as the wavelength selection optics in wide-field imaging spectrometers because they can select a narrow wavelength spectral region to measure a two-dimensional image. This device is then wavelength tuned to measure the hyperspectral image.^[151–153] The major difficulty with these devices is that they generally do not have the required spectral resolution under low loss conditions needed for Raman measurements. Furthermore, these conventional devices do not function in the deep UV.

We recently demonstrated that we can fabricate photonic crystals (PCs) of highly charged monodisperse silica nanoparticles that efficiently diffract narrow wavelength intervals of deep UV light.^[154] These face-centered cubic PCs efficiently diffract a narrow spectral region of UV light that meets the Bragg condition while allowing adjacent wavelengths to transmit.^[155] We demonstrated the use of these deep UV diffracting PCs as Rayleigh rejection filters for 229 nm excited deep UV Raman measurements.^[156]

We also recently demonstrated that our PC devices can be utilized as a wavelength selection optical device to construct a wide-field visible Raman imaging spectrometer.^[60] The PC was utilized to select a narrow spectral region of Raman scattered light from a Teflon sample. We demonstrated proof-of-concept for using PCs as imaging devices in the visible spectral region. We are now utilizing our silica PCs to fabricate a similar deep UV wide-field standoff imaging spectrometer for trace explosive detection.

Conclusion

A number of trace explosive detection methods are currently used in the field. Canine olfaction and IMS are among the most widely used methods for proximity trace explosives detection. There is great interest in developing standoff trace explosive methods in order to prevent terrorist attacks and to protect security personnel. Laser-based spectroscopies appear to be the most promising approaches.

LIBS, CARS, and Raman have recently been investigated for standoff explosive detection. LIBS is promising for elemental analysis, but is less promising for detection of low concentrations of molecular species. LIBS is intrinsically challenged because it is difficult to use as an eye-safe method since pulsed excitation must be used to produce sample dielectric breakdown. CARS standoff spectroscopy with ultrafast lasers has also been examined for standoff detection. Unfortunately, the high pulse powers also make it difficult to use under eye-safe conditions. This may also be true of Raman approaches that use visible or near-IR excitation where high laser power is required to increase spectral S/N.

The advantage of Raman is that the spectra are diagnostic of the molecular structure of the sample. There are unique advantages for using deep UV excitation, which include increased intensities due to the short wavelength excitation, resonance enhancement due to the Raman spectral coupling of vibrational motion with electronic transitions, and the lack of fluorescence interference. Furthermore, the eye damage threshold is higher for deep UV light than for visible and near-IR light.

We are developing standoff deep UVRR methods by investigating resonance enhancement of explosives excited in the deep UV. We determined the optimal excitation wavelengths for detection of numerous explosives. UV excitation causes photochemistry resulting in UVRR spectral changes. We examined the photochemistry of

TNT, RDX, NaNO₃, and NH₄NO₃. We characterized the photochemically induced spectral changes observed in the evolving UVRR spectra. We determined the photoproducts formed during photolysis of TNT, RDX, NaNO₃, and NH₄NO₃. NO₃⁻ and NO₂⁻ are major photochemical products that can be used to confirm the prior presence of explosives. Quantum yields were determined for TNT, RDX, PETN, NaNO₃, and NH₄NO₃ in the solution state as well as for NaNO₃ and NH₄NO₃ in the solid state.

Recent improvements in spectrometers and lasers enabled development of high throughput standoff UV Raman instruments. We estimate a ~100 µg/cm² limit of detection for NaNO₃ with our current high resolution, high throughput Echelle spectrograph at a 2.2 m standoff distance by utilizing a 5 cm diameter collection lens and a 1 min accumulation time.^[112] We are also developing a standoff Raman imaging system for explosives detection that utilizes our recently developed deep UV photonic crystals for wavelength selection.

Acknowledgements

We gratefully acknowledge funding from ONR contract N00014-12-1-0021.

References

- [1] J. S. Caygill, F. Davis, S. P. J. Higson, *Talanta* **2012**, *88*, 0.
- [2] A. W. Fountain, S. D. Christesen, R. P. Moon, J. A. Guicheteau, E. D. Emmons, *Appl. Spectrosc.* **2014**, *68*, 8.
- [3] D. S. Moore, *Sens. Imaging*. **2007**, *8*, 1.
- [4] D. S. Moore, *Rev. Sci. Instrum.* **2004**, *75*, 8.
- [5] P. M. Pellegrino, E. L. Holthoff, M. E. Farrell, in *Laser-based Optical Detection of Explosives* (Ed: K. Iniewski), Taylor & Francis, **2015**.
- [6] J. I. Steinfeld, J. Wormhoudt, *Annu. Rev. Phys. Chem.* **1998**, *49*, 1.
- [7] J. Yinon, *Trac-Trend Anal. Chem.* **2002**, *21*, 4.
- [8] Country Reports on Terrorism 2013: Annex of Statistical Information, National Consortium for the Study of Terrorism and Responses to Terrorism (START), **2014**.
- [9] National Consortium for the Study of Terrorism and Responses to Terrorism (START), Global Terrorism Database [Data File], **2015**. <http://www.start.umd.edu/gtd>
- [10] P. Mostak, M. Standl, in *Detection and Disposal of Improvised Explosives* (Eds: H. Schubert, A. Kuznetsov), Springer Netherlands, **2006**, pp. 33–41.
- [11] C. Wilson, *Improvised explosive devices (IEDs) in Iraq and Afghanistan: effects and countermeasures*, **2006**.
- [12] K. Wells, D. A. Bradley, *Appl. Radiat. Isotopes*. **2012**, *70*, 8.
- [13] M. Marshall, J. C. Oxley, in *Aspects of Explosives Detection* (Eds: M. Marshall, J. C. Oxley), Elsevier, Oxford, **2009**, pp. 11–26.
- [14] H. Östmark, S. Wallin, H. G. Ang, *Propell. Explos. Pyrot.* **2012**, *37*, 1.
- [15] S. Wallin, A. Pettersson, H. Östmark, A. Hobro, *Anal. Bioanal. Chem.* **2009**, *395*, 2.
- [16] P. Kolla, *Angew. Chem. Int. Ed. Engl.* **1997**, *36*, 8.
- [17] A. G. Marshall, J. C. Oxley, in *Aspects of Explosive Detection* (Eds: A. G. Marshall, J. C. Oxley), Elsevier, Oxford, **2009**, p. 1–10.
- [18] K. G. Furton, L. J. Myers, *Talanta*. **2001**, *54*, 3.
- [19] J. C. Oxley, L. P. Waggoner, in *Aspects of Explosive Detection* (Eds: A. G. Marshall, J. C. Oxley), Elsevier, Oxford, **2009**, pp. 27–40.
- [20] K. J. Garner, L. Busbee, P. Cornwell, J. Edmonds, K. Mullins, K. Rader, J. Johnston, J. Williams, *Duty Cycle of the Detector Dog: A Baseline Study*, Institute for Biological Detection Systems, Auburn University, **2001**.
- [21] I. Gazit, J. Terkel, *Appl. Anim. Behav. Sci.* **2003**, *81*, 2.
- [22] L. Lit, J. Schweitzer, A. Oberbauer, *Anim. Cogn.* **2011**, *14*, 3.
- [23] J. Yinon, *Anal. Chem.* **2003**, *75*, 5.
- [24] R. J. Harper, K. G. Furton, in *Counterterrorist Detection Techniques of Explosives* (Ed: J. Yinon), Elsevier, Oxford, **2007**, pp. 395–432.
- [25] R. G. Ewing, C. J. Miller, *Field Anal. Chem. Technol.* **2001**, *5*, 5.
- [26] R. G. Ewing, D. A. Atkinson, G. A. Eiceman, G. J. Ewing, *Talanta*. **2001**, *54*, 3.
- [27] G. A. Eiceman, Z. Karpas, H. H. Hill Jr., *Ion Mobility Spectrometry*, CRC press, Boca Raton, **2013**.

- [28] H. Borsdorf, T. Mayer, M. Zarejousheghani, G. A. Eiceman, *Appl. Spectrosc. Rev.* **2011**, *46*, 6.
- [29] G. Eiceman, *TrAC, Trends Anal. Chem.* **2002**, *21*, 4.
- [30] D. Collins, M. Lee, *Anal. Bioanal. Chem.* **2002**, *372*, 1.
- [31] G. Eiceman, J. Stone, *Anal. Chem.* **2004**, *76*, 21.
- [32] C. K. Hilton, C. A. Krueger, A. J. Midey, M. Osgood, J. Wu, C. Wu, *Int. J. Mass Spectrom* **2010**, *298*, 1–3.
- [33] M. E. Germain, M. J. Knapp, *Chem. Soc. Rev.* **2009**, *38*, 9.
- [34] S. J. Toal, W. C. Troglor, *J. Mater. Chem.* **2006**, *16*, 28.
- [35] J. Almog, S. Zitir, in *Aspects of Explosive Detection* (Eds: A. G. Marshall, J. C. Oxley), Elsevier, Oxford, **2009**, pp. 41–58.
- [36] V. K. Pamula, V. Srinivasan, H. Chakrapani, R. B. Fair, E. J. Toone, *IEEE Int. Conf. Micro Electro Mech. Syst.* **2005**.
- [37] K. L. Bjella, *Pre-screening for Explosives Residues in Soil prior to HPLC Analysis Utilizing Expray Cold Regions Research and Engineering Laboratory*, **2005**.
- [38] Q. Zhou, T. M. Swager, *J. Am. Chem. Soc.* **1995**, *117*, 26.
- [39] Q. Zhou, T. M. Swager, *J. Am. Chem. Soc.* **1995**, *117*, 50.
- [40] T. M. Swager, *Acc. Chem. Res.* **1998**, *31*, 5.
- [41] T. Naddo, Y. Che, W. Zhang, K. Balakrishnan, X. Yang, M. Yen, J. Zhao, J. S. Moore, L. Zang, *J. Am. Chem. Soc.* **2007**, *129*, 22.
- [42] Y. Liu, R. C. Mills, J. M. Boncella, K. S. Schanze, *Langmuir*. **2001**, *17*, 24.
- [43] C.-P. Chang, C.-Y. Chao, J. H. Huang, A.-K. Li, C.-S. Hsu, M.-S. Lin, B. R. Hsieh, A.-C. Su, *Synth. Met.* **2004**, *144*, 3.
- [44] J.-S. Yang, T. M. Swager, *J. Am. Chem. Soc.* **1998**, *120*, 21.
- [45] C. J. Cumming, C. Aker, M. Fisher, M. Fok, M. J. La Grone, D. Reust, M. G. Rockley, T. M. Swager, E. Towers, V. Williams, *IEEE T. Geosci. Remote.* **2001**, *39*, 6.
- [46] T. M. Swager, J. H. Wosnick, *MRS Bull.* **2002**, *27*, 06.
- [47] T. L. Andrew, T. M. Swager, *J. Am. Chem. Soc.* **2007**, *129*, 23.
- [48] M. E. Germain, M. J. Knapp, *Inorg. Chem.* **2008**, *47*, 21.
- [49] Y. Xia, L. Song, C. Zhu, *Anal. Chem.* **2011**, *83*, 4.
- [50] Z. Takáts, I. Cotte-Rodriguez, N. Talaty, H. Chen, R. G. Cooks, *Chem. Commun.* **2005**, 15.
- [51] N. Na, C. Zhang, M. Zhao, S. Zhang, C. Yang, X. Fang, X. Zhang, *J. Mass Spectrom.* **2007**, *42*, 8.
- [52] D. R. Justes, N. Talaty, I. Cotte-Rodriguez, R. G. Cooks, *Chem. Commun.* **2007**, 21.
- [53] A. Buffler, *Radiat. Phys. Chem.* **2004**, *71*, 3.
- [54] R. F. Eilbert, in *Aspects of Explosive Detection* (Eds: A. G. Marshall, J. C. Oxley), Elsevier, Oxford, **2009**, pp. 89–130.
- [55] J. C. Carter, S. M. Angel, M. Lawrence-Snyder, J. Scaffidi, R. E. Whipple, J. G. Reynolds, *Appl. Spectrosc.* **2005**, *59*, 6.
- [56] S. K. Sharma, P. G. Lucey, M. Ghosh, H. W. Hubble, K. A. Horton, *Spectrochim. Acta, Part A.* **2003**, *59*, 10.
- [57] F. J. Fortes, J. J. Laserna, *Spectrochim. Acta, Part B.* **2010**, *65*, 12.
- [58] M. Nelson, P. Treado, in *Raman, Infrared, and Near-infrared Chemical Imaging* (Eds: S. Sasic, Y. Ozaki), John Wiley & Sons, **2011**, pp. 23–51.
- [59] G. Steiner, in *Biomedical Imaging: Principles and Applications* (Ed: R. Salzer), John Wiley & Sons, Hoboken, **2010**, pp. 275–303.
- [60] K. T. Hufziger, S. V. Bykov, S. A. Asher, *Appl. Spectrosc.* **2014**, *68*, 11.
- [61] J. J. Brady, S. D. Roberson, M. E. Farrell, E. L. Holthoff, D. N. Stratis-Cullum, P. M. Pellegrino, in *Laser-induced Breakdown Spectroscopy: A Review of Applied Explosive Detection Army Research Laboratory*, **2013**.
- [62] J. L. Gottfried, F. C. De Lucia Jr, C. A. Munson, A. W. Miziolek, *Anal. Bioanal. Chem.* **2009**, *395*, 2.
- [63] D. W. Hahn, N. Omenetto, *Appl. Spectrosc.* **2010**, *64*, 12.
- [64] D. W. Hahn, N. Omenetto, *Appl. Spectrosc.* **2012**, *66*, 4.
- [65] C. Lopez-Moreno, S. Palanco, J. J. Laserna, F. C. De Lucia, A. W. Miziolek, J. Rose, R. A. Walters, A. I. Whitehouse, *J. Anal. At. Spectrom.* **2006**, *21*, 1.
- [66] J. L. Gottfried, F. C. De Lucia, C. A. Munson, A. W. Miziolek, *J. Anal. At. Spectrom.* **2008**, *23*, 2.
- [67] J. L. Gottfried, F. C. De Lucia, *Imaging and applied optics technical papers*, **2012**.
- [68] J. L. Gottfried, *Appl. Opt.* **2013**, *52*, 4.
- [69] P. Lucena, I. Gaona, J. Moros, J. J. Laserna, *Spectrochim. Acta, Part B.* **2013**, *85*, 0.
- [70] R. González, P. Lucena, L. Tobaría, J. Laserna, *J. Anal. At. Spectrom.* **2009**, *24*, 8.
- [71] J. Moros, J. Lorenzo, J. Laserna, *Anal. Bioanal. Chem.* **2011**, *400*, 10.
- [72] S. A. Oladepo, K. Xiong, Z. Hong, S. A. Asher, J. Handen, I. K. Lednev, *Chem. Rev.* **2012**, *112*, 5.
- [73] S. A. Asher, in *Handbook of Vibrational Spectroscopy* (Eds: J. M. Chalmers, P. R. Griffiths), J. Wiley, **2002**, pp. 1–15.
- [74] S. A. Asher, *Anal. Chem.* **1993**, *65*, 2.
- [75] S. Angel, T. J. Kulp, T. M. Vess, *Appl. Spectrosc.* **1992**, *46*, 7.
- [76] S. K. Sharma, A. K. Misra, B. Sharma, *Spectrochim. Acta, Part A.* **2005**, *61*, 10.
- [77] H. Östmark, M. Nordberg, T. E. Carlsson, *Appl. Opt.* **2011**, *50*, 28.
- [78] A. Pettersson, I. Johansson, S. Wallin, M. Nordberg, H. Östmark, *Propellants, Explos. Pyrotech.* **2009**, *34*, 4.
- [79] B. Zachhuber, C. Gasser, E. T. H. Chrysostom, B. Lendl, *Anal. Chem.* **2011**, *83*, 24.
- [80] P. Matousek, I. Clark, E. Draper, M. Morris, A. Goodship, N. Everall, M. Towrie, W. Finney, A. Parker, *Appl. Spectrosc.* **2005**, *59*, 4.
- [81] B. Zachhuber, H. Östmark and T. Carlsson, Proc. SPIE 9073, Chemical, Biological, Radiological, Nuclear, and Explosives (CBRNE) Sensing XV, **2014**.
- [82] A. K. Misra, S. K. Sharma, T. E. Acosta, J. N. Porter, D. E. Bates, *Appl. Spectrosc.* **2012**, *66*, 11.
- [83] M. T. Bremer, P. J. Wrzesinski, N. Butcher, V. V. Lozovoy, M. Dantus, *Appl. Phys. Lett.* **2011**, *99*, 10.
- [84] O. Katz, A. Natan, Y. Silberberg, S. Rosenwaks, *Appl. Phys. Lett.* **2008**, *92*, 17.
- [85] A. Natan, J. M. Levitt, L. Graham, O. Katz, Y. Silberberg, *Appl. Phys. Lett.* **2012**, *100*, 5.
- [86] J.-X. Cheng, X. S. Xie, *J. Phys. Chem. B* **2004**, *108*, 3.
- [87] W. M. Tolles, J. W. Nibler, J. R. McDonald, A. B. Harvey, *Appl. Spectrosc.* **1977**, *31*, 4.
- [88] N. Dudovich, D. Oron, Y. Silberberg, *Nature* **2002**, *418*, 6897.
- [89] S. Asher, C. Johnson, *Science* **1984**, *225*, 4659.
- [90] E. D. Emmons, A. Tripathi, J. A. Guicheteau, A. W. Fountain, S. D. Christesen, *J. Phys. Chem. A* **2013**, *117*, 20.
- [91] J. A. Carroll, E. L. Izake, B. Cletus, E. Jaatinen, *J. Raman Spectrosc.* **2015**, *46*, 3.
- [92] D. D. Tuschel, A. V. Mikhonin, B. E. Lemoff, S. A. Asher, *Appl. Spectrosc.* **2010**, *64*, 4.
- [93] M. Ghosh, L. Wang, S. A. Asher, *Appl. Spectrosc.* **2012**, *66*, 9.
- [94] S. A. Asher, D. D. Tuschel, T. A. Vargson, L. Wang, S. J. Geib, *J. Phys. Chem. A* **2011**, *115*, 17.
- [95] K. L. Gares, S. V. Bykov, B. Godugu, S. A. Asher, *Appl. Spectrosc.* **2014**, *68*, 1.
- [96] L. Nagli, M. Gaft, Y. Flegler, M. Rosenbluh, *Opt. Mater.* **2008**, *30*, 11.
- [97] Z. Hong, S. A. Asher, *Appl. Spectrosc.* **2015**, *69*, 1.
- [98] W. A. Al-Saidi, S. A. Asher, P. Norman, *J. Phys. Chem. A* **2012**, *116*, 30.
- [99] K. L. Gares, S. V. Bykov, T. Brinzer, S. A. Asher, *Appl. Spectrosc.* **2015**, *69*, 5.
- [100] L. Wang, D. Tuschel and S. A. Asher, Proc. SPIE 8018, Chemical, Biological, Radiological, Nuclear, and Explosives (CBRNE) Sensing XII, **2011**.
- [101] L. Wang, D. Tuschel, S. A. Asher, *J. Phys. Chem. C* **2011**, *115*, 32.
- [102] E. D. Emmons, J. A. Guicheteau, A. W. Fountain, S. D. Christesen, *Appl. Spectrosc.* **2012**, *66*, 6.
- [103] T. L. Andrew, T. M. Swager, *J. Org. Chem.* **2011**, *76*, 9.
- [104] J. C. Sanchez, W. C. Troglor, *J. Mater. Chem.* **2008**, *18*, 26.
- [105] M. L. Clark, M. J. Aernecke, K. E. Gregory, D. E. Hardy, R. R. Kunz, *Sensing Impacts of the Fate of Trace Explosives Signatures under Environmental Conditions*, Edgewood Chemical Biological Center, **2010**.
- [106] R. R. Kunz, K. E. Gregory, M. J. Aernecke, M. L. Clark, A. Ostrinskaya, A. W. Fountain 3rd, *J. Phys. Chem. A* **2012**, *116*, 14.
- [107] J. C. Pennington, K. A. Thorn, L. G. Cox, D. K. MacMillan, S. Yost, R. D. Laubscher, *Photochemical Degradation of Composition B and Its Components*, Engineer Research and Development Center, **2007**.
- [108] M. Greenfield, Y. Q. Guo, E. R. Bernstein, *Chem. Phys. Lett.* **2006**, *430*, 4–6.
- [109] H.-S. Im, E. R. Bernstein, *J. Chem. Phys.* **2000**, *113*, 18.
- [110] G. R. Peyton, M. H. LeFavre, S. W. Maloney, *Verification of RDX Photolysis Mechanism*, Engineer Research and Development Center, **1999**.
- [111] A. F. Smetana, S. Bulusu, *Photochemical Studies of Secondary Nitramines. Part 2. Ultraviolet Photolysis and Ozonolysis of RDX in Aqueous Solutions*, Large Caliber Weapons Systems Laboratory, **1977**.
- [112] S. V. Bykov, M. Mao, K. L. Gares, S. A. Asher, *Appl. Spectrosc.* **2015**, *69*, 8.
- [113] K. L. Gares, S. V. Bykov and S. A. Asher, (paper in progress). **2015**.
- [114] M. Daniels, R. Meyers, E. Belardo, *J. Phys. Chem.* **1968**, *72*, 2.
- [115] J. Mack, J. R. Bolton, *J. Photochem. Photobiol. A* **1999**, *128*, 1–3.

- [116] G. Mark, H.-G. Korth, H.-P. Schuchmann, C. von Sonntag, *J. Photochem. Photobiol. A*, **1996**, *101*, 2–3.
- [117] U. Shuali, M. Ottolenghi, J. Rabani, Z. Yelin, *J. Phys. Chem.* **1969**, *73*, 10.
- [118] J. Clarkson, W. E. Smith, D. N. Batchelder, D. A. Smith, A. M. Coats, *J. Mol. Struct.* **2003**, *648*, 3.
- [119] H. Wackerbath, L. Gundrum, C. Salb, K. Christou, W. Viol, *Appl. Opt.* **2010**, *49*, 23.
- [120] D. J. Glover, J. C. Hoffsommer, *Photolysis of RDX in Aqueous Solution, with and without Ozone*, Naval Surface Weapons Center, **1979**.
- [121] Y. Q. Guo, M. Greenfield, A. Bhattacharya, E. R. Bernstein, *J. Chem. Phys.* **2007**, *127*, 15.
- [122] N. J. Harris, K. Lammertsma, *J. Am. Chem. Soc.* **1997**, *119*, 28.
- [123] Z. A. Dreger, Y. M. Gupta, *J. Phys. Chem. B* **2007**, *111*, 15.
- [124] R. J. Spangford, T. Mill, T.-W. Chou, W. R. Mabey, J. H. Smith, *Environmental Fate Studies on Certain Munition Wastewater Constituents-Laboratory Studies*, SRI International, **1980**.
- [125] A. C. Ferrari, S. E. Rodil, J. Robertson, *Phys. Rev. B* **2003**, *67*, 15.
- [126] P. F. McMillan, V. Lees, E. Quirico, G. Montagnac, A. Sella, B. Reynard, P. Simon, E. Bailey, M. Deifallah, F. Corà, *J. Solid State Chem.* **2009**, *182*, 10.
- [127] S. E. Rodil, A. C. Ferrari, J. Robertson, S. Muhl, *Thin Solid Films* **2002**, *420–421*, 0.
- [128] S. S. Roy, R. McCann, P. Papakonstantinou, P. Maguire, J. A. McLaughlin, *Thin Solid Films* **2005**, *482*, 1–2.
- [129] A. K. M. S. Chowdhury, D. C. Cameron, M. S. J. Hashmi, *Thin Solid Films* **1998**, *332*, 1–2.
- [130] S. Chaturvedi, P. N. Dave, *J. Energ. Mater.* **2013**, *31*, 1.
- [131] G. Feick, R. M. Hainer, *J. Am. Chem. Soc.* **1954**, *76*, 22.
- [132] J. C. Oxley, S. M. Kaushik, N. S. Gilson, *Thermochim. Acta.* **1989**, *153*, 0.
- [133] A. J. B. Robertson, *J. Soc. Chem. Ind.* **1948**, *67*, 6.
- [134] W. A. Rosser, S. H. Inami, H. Wise, *J. Phys. Chem.* **1963**, *67*, 9.
- [135] S. Goldstein, J. Rabani, *J. Am. Chem. Soc.* **2007**, *129*, 34.
- [136] D. Chambers, *Perspectives on Pentaerythritol Tetranitrate (PETN) Decomposition*, Lawrence Livermore National Laboratory, **2002**.
- [137] W. Ng, J. Field, H. Hauser, *J. Appl. Phys.* **1986**, *59*, 12.
- [138] B. D. Roos, T. B. Brill, *Combust. Flame.* **2002**, *128*, 1–2.
- [139] M. A. Hiskey, K. R. Brower, J. C. Oxley, *J. Phys. Chem.* **1991**, *95*, 10.
- [140] M. R. Almeida, D. N. Correa, J. J. Zacca, L. P. L. Logrado, R. J. Poppi, *Anal. Chim. Acta* **2015**, *860*.
- [141] R. Bhartia, W. F. Hug, R. D. Reid, Proc. SPIE 8358, Chemical, Biological, Radiological, Nuclear, and Explosives (CBRNE) Sensing XIII, **2012**.
- [142] W. F. Hug, R. Bhartia, K. Sijapati, L. Beegle, R. Reid, Proc. SPIE 9073, Chemical, Biological, Radiological, Nuclear, and Explosives (CBRNE) Sensing XV, **2014**.
- [143] R. Bhartia, W. F. Hug, R. D. Reid, L. W. Beegle, in *Laser-based Optical Detection of Explosives* (Ed: K. Iniewski), Taylor & Francis, Boca Raton, **2015**, pp. 67–98.
- [144] R. Waterbury, J. Rose, D. Vunck, T. Blank, K. Pohl, A. Ford, T. McVay, E. Dottery, Proc. SPIE 8018 Chemical, Biological, Radiological, Nuclear, and Explosives (CBRNE) Sensing XIII, **2011**.
- [145] A. Ehlerding, I. Johansson, S. Wallin, H. Östmark, *Int. J. Spectrosc.* **2012**, *2012*.
- [146] T. A. Reichardt, S. E. Bisson, T. J. Kulp, *Standoff Ultraviolet Raman Scattering Detection of Trace Levels of Explosives*, Sandia National Labs, **2011**.
- [147] S. V. Bykov, B. Sharma, S. A. Asher, *Appl. Spectrosc.* **2013**, *67*, 8.
- [148] S. V. Bykov, I. Lednev, A. Ianoul, A. Mikhonin, C. Munro, S. A. Asher, *Appl. Spectrosc.* **2005**, *59*, 12.
- [149] G. Puppels, M. Grond, J. Greve, *Appl. Spectrosc.* **1993**, *47*, 8.
- [150] M. Nelson, P. Treado, R. Priore, Patent US20100265502 A1, **2010**.
- [151] H. R. Morris, C. C. Hoyt, P. J. Treado, *Appl. Spectrosc.* **1994**, *48*, 7.
- [152] M. Iga, N. Kakuryu, T. Tanaami, J. Sajiki, K. Isozaki, T. Itoh, *Rev. Sci. Instrum.* **2012**, *83*, 10.
- [153] H. R. Morris, C. C. Hoyt, P. Miller, P. J. Treado, *Appl. Spectrosc.* **1996**, *50*, 6.
- [154] S. A. Asher, L. Wang, D. Tuschel, Patent US20120062883 A1, **2011**.
- [155] S. A. Asher, J. M. Weissman, A. Tikhonov, R. D. Coalson, R. Kesavamoorthy, *Phys. Rev. E Stat. Nonlinear Soft Matter Phys.* **2004**, *69*, 6.
- [156] L. Wang, A. Tikhonov, S. A. Asher, *Appl. Spectrosc.* **2012**, *66*, 4.